nature chemical biology

Article

https://doi.org/10.1038/s41589-025-01891-7

Monitoring in real time and far-red imaging of H_2O_2 dynamics with subcellular resolution

Received: 26 February 2024

Accepted: 25 March 2025

Justin Daho Lee[1,2,3], Amanda Nguyen[2], Chelsea E. Gibbs[2,13], Zheyu Ruby Jin[4,13], Yuxuan Wang[2,13], Aida Moghadasi[2], Sarah J. Wait[1,2,3], Hojun Choi[5,6], Kira M. Evitts[2,3], Anthony Asencio[2,3,7,8], Samantha B. Bremner[2], Shani Zuniga[2], Vedant Chavan[2], Inez K. A. Pranoto[3,9], C. Andrew Williams[3,9], Annette Smith[3], Farid Moussavi-Harami[3,7,8,9,10], Michael Regnier[2,3,7,8], David Baker[5,6,11], Jessica E. Young[3,9], David L. Mack[2,3,12], Elizabeth Nance[1,2,4], Patrick M. Boyle[2,3,7,8] & Andre Berndt[1,2,3,7] ✉

Monitoring H_2O_2 dynamics in conjunction with key biological interactants is critical for elucidating the physiological outcome of cellular redox regulation. Optogenetic hydrogen peroxide sensor with HaloTag with JF635 (oROS-HT_{635}) allows fast and sensitive chemigenetic far-red H_2O_2 imaging while overcoming drawbacks of existing red fluorescent H_2O_2 indicators, including oxygen dependency, high pH sensitivity, photoartifacts and intracellular aggregation. The compatibility of oROS-HT_{635} with blue-green-shifted optical tools allows versatile optogenetic dissection of redox biology. In addition, targeted expression of oROS-HT_{635} and multiplexed H_2O_2 imaging enables spatially resolved imaging of H_2O_2 targeting the plasma membrane and neighboring cells. Here we present multiplexed use cases of oROS-HT_{635} with other green fluorescence reporters by capturing acute and real-time changes in H_2O_2 with intracellular redox potential and Ca^{2+} levels in response to auranofin, an inhibitor of antioxidative enzymes, via dual-color imaging. oROS-HT_{635} enables detailed insights into intricate intracellular and intercellular H_2O_2 dynamics, along with their interactants, through spatially resolved, far-red H_2O_2 imaging in real time.

Oxidative stress is often a key component of many disease progressions. Tremendous efforts have been made to develop therapeutic approaches to target the excessive presence of oxidants and their sources. However, the unsatisfying results of antioxidative therapy call for a more nuanced understanding of cellular oxidants, antioxidative defense networks and their effects on cellular systems with precision and specificity to improve rationales for the development of antioxidative therapeutics[1].

H_2O_2 is a major oxidant in redox biology that can also act as a pleiotropic secondary messenger in various cellular signaling processes[2–6] and is tightly regulated[7,8]. Its precursor O_2^- is a natural by-product of aerobic metabolism, which rapidly gets converted to H_2O_2 naturally or by superoxide dismutase[9]. Flavin-containing oxidases are also another important source of H_2O_2 (ref. 10). Excessive accumulation of H_2O_2 is often observed in pathology, with growing evidence of its causal role in the progression of diseases[11–13]. Genetically encoded H_2O_2 indicators (GEHI; for example, OxyR-based sensors[14–16] and peroxidase-based sensors[17–19]) enable real-time monitoring of H_2O_2 dynamics in a wide array of biological hosts[20]. Specifically, red fluorescent GEHIs facilitate multiparametric analysis of H_2O_2 dynamics along with other key biomolecules or processes, considering a large number of green fluorescent sensors for biological molecules and processes (for example, Ca^{2+}, pH, voltage, redox potential and so on)[21,22]. Nevertheless, current red-shifted GEHIs exhibit slow kinetics, a bottleneck for real-time H_2O_2 imaging. Most importantly, blue-light-induced photochromic artifacts commonly associated with red fluorescent protein (FP)-based sensors

A full list of affiliations appears at the end of the paper. ✉e-mail: berndtuw@uw.edu

can cause false signals in polychromatic imaging when used alongside green fluorescent sensors[23]. Last, aggregation tendency and low brightness are also observed among red FPs (RFPs)[24], thus diminishing the utility of existing red GEHIs. OxyR is a bacterial transcription activator with high specificity and sensitivity toward H_2O_2 with low peroxidative capabilities (that is, the protein exhibits high sensitivity toward H_2O_2 with limited catalytic activity)[25]. Existing red-shifted GEHIs, such as HyPerRed[15] and SHIRMP[16], use ecOxyR-LBD (the ligand binding domain of OxyR from *Escherichia coli*) as their sensing domain. However, both red GEHIs show slower kinetics (10 s to 100 s for full activation under saturation and 30 min for reduction) than the innate kinetics and sensitivity reported for ecOxyR itself[26–28]. Specifically, the rate of ecOxyR oxidation is at a subsecond scale, and its reduction takes 5–10 min. We hypothesized that the insertion of the fluorescence reporter domain may have slowed the activation and deactivation of ecOxyR in the currently available red-shifted GEHI sensors.

In this study, we couple the bacterial OxyR H_2O_2 sensor with a rhodamine-HaloTag-based chemigenetic reporter system to create a far-red indicator for H_2O_2, named optogenetic hydrogen peroxide sensor with HaloTag with Janelia Fluorophore 635 (JF635; oROS-HT_{635}). We develop a rational engineering strategy based on structural information derived from experimentally resolved structures and computational models (ColabFold)[29], which leads to a bright and fast far-red sensor that allows for the observation of intracellular diffusion of H_2O_2 with high sensitivity. Also, oROS-HT_{635} is free from photochromic artifacts, allowing polychromatic analysis of contextual H_2O_2 dynamics. As a proof of concept, we show the acute effect of the anti-inflammatory agent auranofin on H_2O_2 levels together with changes in cellular redox potential in HEK293 cells or Ca^{2+} levels in human-induced pluripotent stem cell-derived cardiomyocytes (hiPS cell-CMs). These experiments establish more accurate spatial and temporal correlations between different physiological phenomena. Last, we present chemogenetic and optogenetic methods of visualizing site-specific H_2O_2 generation and diffusion from mitochondria and outer plasma membranes to the inner plasma membrane and neighboring cells.

Results

Engineering a bright far-red chemigenetic sensor for H_2O_2

Our engineering strategy aimed to maintain the flexibility of the protein loop that drives the conformational change in the sensing domain (that is, ecOxyR-LBD) in the derived sensors, as we previously validated in the development of a green FP (GFP)-based oROS-G sensor[30]. Specifically, ecOxyR contains a hydrophobic pocket that forms the active center for H_2O_2 interactions. After binding, H_2O_2 forms a hydrogen bonding network with adjacent residues, bringing residues C199 and C208 into close proximity to form a disulfide bridge. By analyzing the B-factors of ecOxyR-LBD structures, we observed an evident high flexibility peak in the 199–208 region (Fig. 1a). We reasoned that preserving this flexibility is necessary for efficient OxyR activation by H_2O_2 (refs. 25,31,32). Thus, inserting a bulky fluorescent reporter between C199 and C208, as in HyPerRed, may be responsible for the slowed OxyR activation, and we explored alternatives outside this region (Fig. 1b). Furthermore, RFPs pose challenges for versatile use involving optical polychromatic analysis or neuron expression. For example, circularly permuted mApple (cpmApple), used in HyPerRed, exhibits a false-positive photochromic artifact induced by blue light commonly used to excite GFPs (for example, 488 nm)[23] and neuronal aggregation[33].

Deo et al. proposed a chemigenetic solution for designing optogenetic sensors that entails incorporating a self-labeling enzyme (HaloTag) with an irreversible conjugation of rhodamine-based JF[34,35]. Red- to far-red-shifted JFs exhibit exceptional photophysical characteristics such as brightness and photostability, which surpass existing RFPs. We aimed to engineer a class of GEHIs using cpHaloTag labeled with the far-red fluorescent JF635 as a reporter domain. Insertion of cpHaloTag into multiple positions outside of the C199–C208 loop in ecOxyR showed accelerated responses to 300 μM H_2O_2 in contrast to the variant with 205–206 insertion, demonstrating improved sensor kinetics associated with an alternative domain insertion strategy, and we identified a prototype sensor variant with insertion at 213–214 with a robust response to bolus 300 μM H_2O_2 ($\Delta F/F_0$: −38.29%; confidence interval (CI) = −40.44, −36.19; time 9–95% (s): 4.05; CI = 3.72, 4.42; Fig. 1c,d). Interestingly, we observed inverse responses (for example, an increase in H_2O_2 levels leads to decreased fluorescence) to H_2O_2 in all cpHaloTag insertions outside of the C199–C208 loop. Therefore, we prioritized improving the brightness, guided by structures predicted from ColabFold (AlphaFold2 with MMseqs2 for multiple sequence alignment)[29]. The prediction yielded a highly confident structure of variant 213–214, exemplified by a dimeric interface of the sensing domain that closely resembles the dimeric interface of reduced ecOxyR resolved by crystallography (Supplementary Fig. 1a,b). We superimposed the cpHaloTag-JF635 structure from Protein Data Bank (PDB) 6U2M to identify the putative position of JF635 with the sensing domain of variant 213–214 (Supplementary Fig. 1c). The prediction showed 'exposed' domain positioning, where the OxyR sensing domain was oriented away from JF635 rather than enclosing the JF635 fluorophore (Fig. 1e and Supplementary Fig. 2), increasing the potential influence of interdomain linker regions on the fluorophore's local environment. This configuration (Supplementary Figs. 1b and 2) is consistent with the spatial configuration of the chemigenetic Ca^{2+} indicator HaloCaMP1b[34].

Consequently, random mutagenesis of interdomain linker residues (XX-cpHaloTag-X, where X indicates mutagenesis targets) affected both the sensor brightness and dynamic range (Fig. 1f). From the linker variant library, we found a variant (TG-cpHaloTag-R) with 8.9-fold increased resting brightness and a 27% increase in dynamic range induced by 300 μM H_2O_2 compared to variant 213–214 (normalized brightness of 213–214: 1.00, CI = 0.89, 1.14; TG-cpHaloTag-R: 8.93, CI = 7.29, 10.63; normalized $\Delta F/F_0$ of variant 213–214: −1.0 (n = 1,468), CI = −1.04, −0.96; dynamic range of TG-cpHaloTag-R: −1.27 (n = 2,668), CI = −1.27, −1.26), which was later named oROS-HT_{635} (Fig. 1g). In addition to the structural hypothesis of the interdomain linker's influence on both sensor dynamics and brightness, we also identified F209 to be a putative mutational site for fluorophore local environment tuning, resulting in a more than threefold difference in resting brightness between the dimmest variant (F209L) and the brightest variant (F209R), and the trend was also consistent when the sensor was labeled with ligand JF585. Unfortunately, the mutational benefits of TG-cpHaloTag-R and F209R were nonsynergistic, which led us to exclude mutation F209R for our final variant (Supplementary Fig. 3a–d).

Highly sensitive, fast and bright far-red H_2O_2 sensor

We first characterized oROS-HT_{635} by exogenously applying H_2O_2 to cells expressing the sensor and then by applying menadione, which induces intracellular H_2O_2 generation. Menadione generates H_2O_2 through various redox cycling mechanisms[36–39] (Supplementary Fig. 4a). Saturation of oROS-HT_{635} induced by 300 μM H_2O_2 revealed a fast subsecond activation that could capture extracellular H_2O_2 diffusion across the imaging field of view. This implies that the kinetic efficiency of the sensor passed a milestone of no longer being reaction limited in this scenario. Intriguingly, the response amplitude of oROS-HT_{635} at 10 μM external H_2O_2 was −58.69% $\Delta F/F_0$ (CI = −59.18, −58.18), which is 87% of the amplitude at saturation following treatment with 300 μM H_2O_2 (−67.27% $\Delta F/F_0$; CI = −67.64, −66.91), demonstrating the exceptional sensitivity of the sensor (Supplementary Fig. 4b) compared to previously reported red GEHIs. Previous studies showed the intracellular H_2O_2 concentrations in HEK293 cells are at approximately 10 and 300 nM under these external conditions, respectively[2,15]. Moreover, we titrated extracellular H_2O_2 as a sensitivity benchmark and found that oROS-HT_{635} is more sensitive than HyPerRed and HyPer7 (ref. 14), a green fluorescent H_2O_2 sensor (Fig. 2a). Furthermore, oROS-HT_{635} allowed the monitoring of titrated H_2O_2 levels in HEK293 cells induced by 10, 20 and 50 μM menadione. We

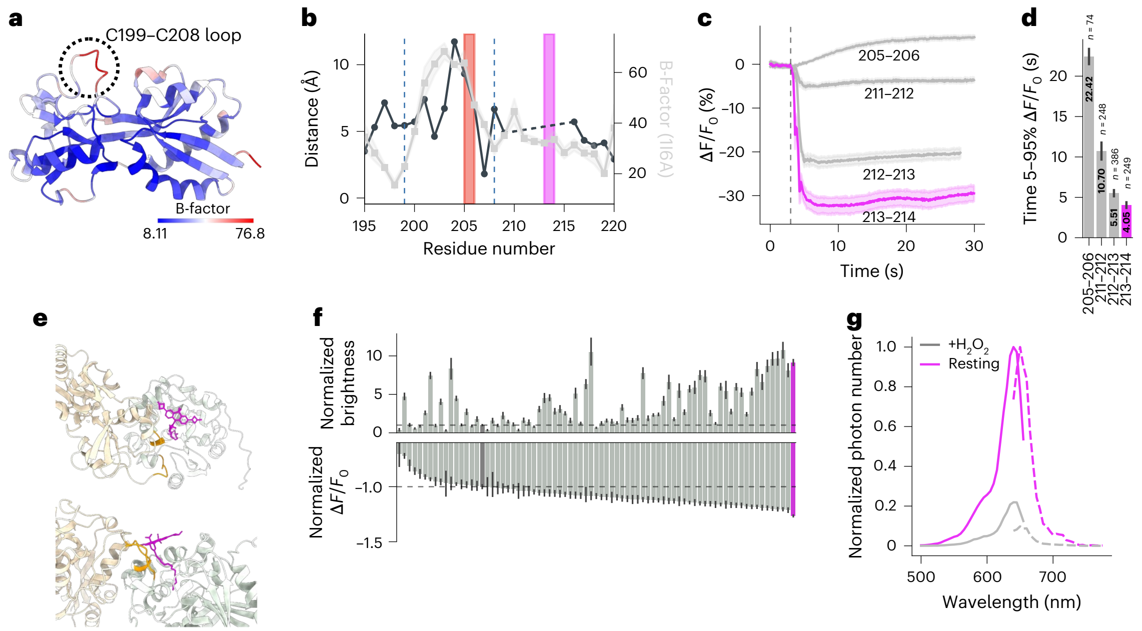

Fig. 1 | Structure-guided engineering of oROS-HT$_{635}$: bright far-red optogenetic sensor for H_2O_2. **a**, B-factor of the regulatory domain of the oxidized form of ecOxyR (PDB ID 1I6A) indicates flexible (red) and rigid (blue) regions. **b**, Pairwise distance between residues 195 and 220 of oxidized (PDB ID 1I6A) and reduced (PDB ID 1I69) crystal structures of the ecOxyR regulatory domain (gray line) indicate intramolecular dynamics induced by H_2O_2 binding. The average B-factor of residues 195 to 220 in the oxidized ecOxyR regulatory domain (PDB ID 1I6A; black line) is also shown. The dashed lines indicate C199 and C208. The red and magenta bars indicate the reporter insertion sites in HyPerRed (cpmApple) and oROS-HT (cpHaloTag), respectively. **c**, Prototype variants of oROS-HT$_{635}$ from cpHaloTag (cpHaloTag7, from HaloCaMP1a) insertional screening between residues 211 and 214 of ecOxyR. Fluorescence change ($\Delta F/F_0$) in response to extracellular H_2O_2 (300 µM) stimulation of the variants expressed in HEK293 cells. **d**, Kinetics of variants depicted in **c** shown as time for the change in fluorescence from 5 to 95% $\Delta F/F_0$. **e**, Putative JF635 dye position bound to cpHaloTag (gray) in the predicted oROS-HT structure. The predicted structure of the 213–214 cpHaloTag variant was superimposed with the cpHaloTag crystal structure (PDB ID 6U2M) to obtain a relative position of JF635 on the 213–214 cpHaloTag variant (gray, cpHaloTag; beige, OxyR; orange, linkers; magenta, JF635-HTL). **f**, Random linker mutagenesis screening of interdomain linkers (X-cpHaloTag-XX) in HEK293 cells. Top: normalized brightness (213–214 variant at 1.0) of each sensor variant. Bottom: normalized $\Delta F/F_0$ (213–214 variant at −1.0) of each sensor variant with 300 µM H_2O_2 stimulation. Statistical information for each variant is available in Supplementary Table 1 (magenta, oROS-HT; dark gray, variant 211–212; dashed lines, mean of 211–212). **g**, Spectral profile of oROS-HT expressed in HEK293 cells. The solid line indicates the excitation spectra (peak: 640 nm), and the dotted line indicates the emission spectra (peak: 650 nm). Error bars and bands in the plots represent the 95% bootstrap (n = 1,000) CI of the mean calculated using the statistical plotting package Seaborn (v0.13.2).

measured a concentration-dependent response in oROS-HT$_{635}$ signal of −26.8% $\Delta F/F_0$ (CI = −27.63, −25.98), −59.59% $\Delta F/F_0$ (CI = −60.48, −58.67) and −63.06% $\Delta F/F_0$ (CI = −63.59, −62.51), respectively (Supplementary Fig. 4c). Interestingly, under 50 µM menadione, oROS-HT$_{635}$ reaches near-maximum fluorescence amplitudes but at much slower rates than exogenously induced instant H_2O_2 saturation (300 µM). Therefore, these kinetics most likely show the real-time increase of cytosolic H_2O_2 by menadione.

Additionally, oROS-HT$_{635}$ response kinetics were faster under saturating 300 µM H_2O_2 than HyPerRed (5–95% |$\Delta F/F_0$| time, oROS-HT$_{635}$: 2.11 s, CI = 1.85, 2.37; HyPerRed: 25.22 s, CI = 22.5, 28.37; Fig. 2b). Many experimental studies of intracellular H_2O_2 often assume well-mixed uniformity of H_2O_2 concentrations[20,40]. However, a previous model for cytosolic H_2O_2 also showed that spatial H_2O_2 gradients in mammalian cells can emerge following external H_2O_2 stimulation[40]. Exceptional kinetics of oROS-HT$_{635}$ demonstrated spatial H_2O_2 diffusion in the cytoplasm of cardiomyocytes when exposed to a bolus of 300 µM H_2O_2 with subcellular resolution (Fig. 2c).

Next, we measured brightness when expressed in cells because several studies indicate discrepancies between in vitro and cellular brightness[41,42]. First, we fused enhanced GFP (eGFP) to the C terminus of both sensors as a reference for fluorescence output. We conducted lambda scans across the visible spectrum using a confocal microscope with a white-light laser. The detector system provided accurate photon counting with minimal dead time[43]. We measured each sensor's cellular brightness by normalizing photon counts at reduced and oxidized states to the photon count of their fused eGFP reference. Importantly, we excited eGFP, HyPerRed and oROS-HT$_{635}$ at an equivalent laser power (49 µW; Fig. 2d). Based on the normalized photon count, the dimmest (for example, oxidized) state of oROS-HT$_{635}$ was ~20-fold brighter than the brightest (for example, reduced) state of HyPerRed (Fig. 2e,f). In addition, oROS-HT$_{635}$ displayed a narrower emission spectrum than HyPerRed, making it ideal for efficient spectral separation in multicolor imaging. The full-width at half-maximum was ~34 nm for oROS-HT$_{635}$ and ~104 nm for HyperRed (Fig. 2g). In addition, oROS-HT$_{635}$ showed a better quantum efficiency (0.216) than existing far-red-shifted fluorescent proteins[44]. oROS-HT$_{635}$ also displayed robust expression in various mammalian tissues (for example, primary rat cortical neurons and ex vivo rat brain tissue) and human stem cell-derived models (for example, cardiomyocytes and cortical neurons; Fig. 2h). Specifically, oROS-HT$_{635}$ expressed in cells did not produce noticeable aggregates, as often found in RFP-based indicators[45–47]. oROS-HT$_{635}$ also displayed higher levels of monomericity than HyPerRed, as shown by our organized smooth endoplasmic reticulum (OSER)[48] assay (Supplementary Fig. 5). Last, oROS-HT$_{635}$ could be repeatedly activated and reduced back to baseline by serial H_2O_2 stimulation and washout, demonstrating the reversibility of the sensor. Thus, the sensor can track real-time fluctuations in intracellular H_2O_2 (Supplementary Fig. 6).

Environmentally stable real-time H_2O_2 imaging

We envision users of oROS-HT$_{635}$ studying H_2O_2 dynamics under varying conditions. Thus, we further characterized notable

https://doi.org/10.1038/s41589-025-01891-7

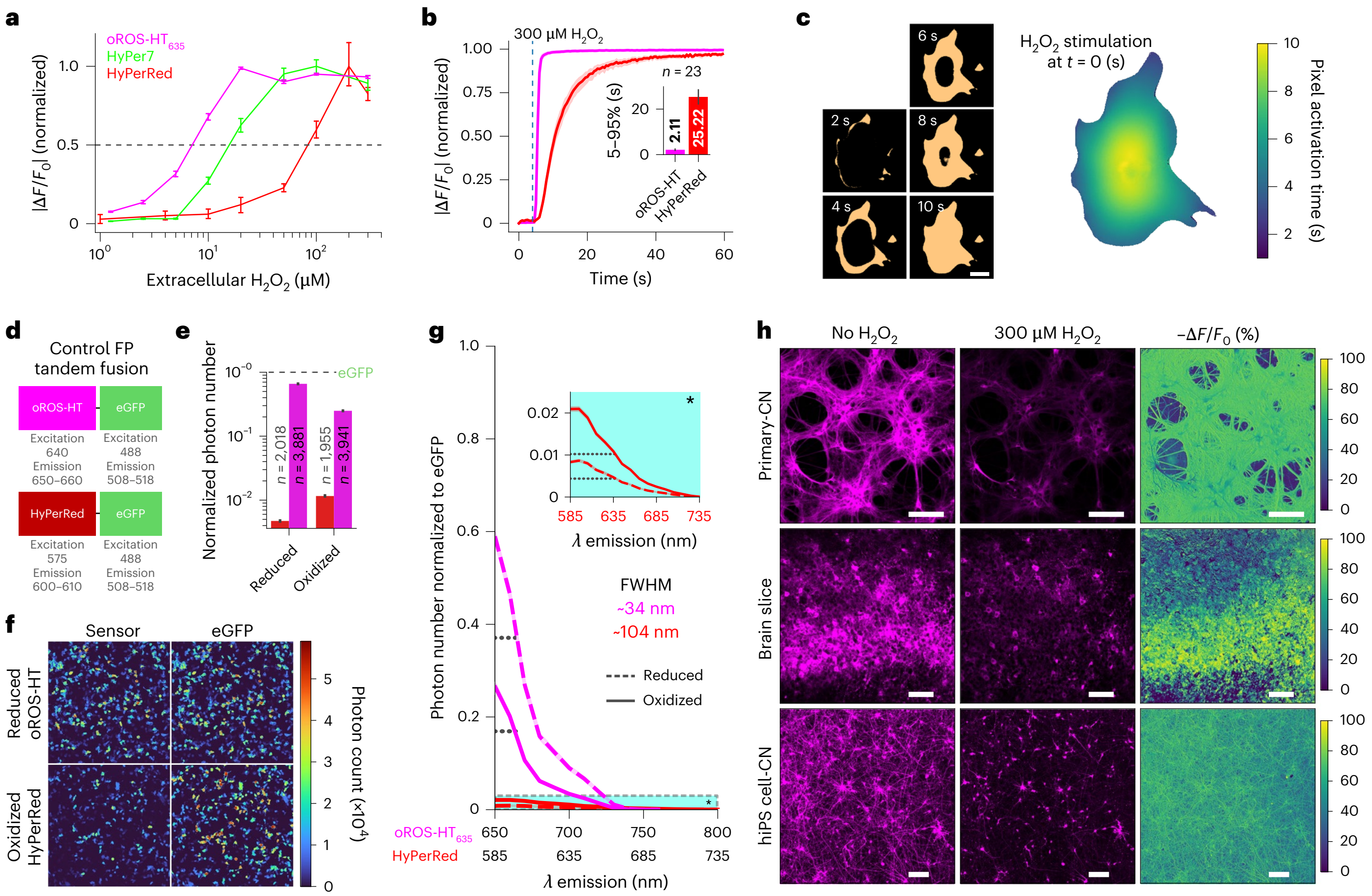

Fig. 2 | Characterization of oROS-HT$_{635}$: a bright, sensitive and fast H_2O_2 sensor. a, H_2O_2 sensitivity benchmarking of oROS-HT$_{635}$, HyPer7 and HyPerRed using extracellular H_2O_2 titration. Each sensor was expressed in HEK293 cells. Fluorescence responses ($\Delta F/F_0$) were scaled to the highest response observed (among all H_2O_2 conditions, $n > 100$ cells for each concentration/sensor for 3 wells). **b**, Normalized response of oROS-HT$_{635}$ and HyPerRed to exogenous 300 μM H_2O_2 ($n = 23$ cells per sensor). Inset: the time for change in fluorescence from 5 to 95% $\Delta F/F_0$. **c**, Intracellular diffusion of H_2O_2 across a hiPS cell-CM expressing oROS-HT$_{635}$ captured at a 20-Hz frame rate following 300 μM H_2O_2 extracellular administration. Left: in the image series, pixel values are Boolean gated for 50% or above sensor activation to enhance contrast for H_2O_2 diffusion; scale bar, 50 μm. Right: diffusion map representing pixel-wise activation time(s). **d**, Assessment of relative cellular brightness with eGFP fused to H_2O_2 sensors as a reference. **e**, Photon counts reported for each sensor's emission window (at a width of 10 nm) were normalized to corresponding eGFP photon counts from the same measurement. 'Reduced' indicates photon counts at the resting state. 'Oxidized' indicates photon counts after 300 μM H_2O_2 stimulation. Ratios were log transformed for enhanced visual comparison (four wells and three images per construct). **f**, Representative raw images of each tandem fusion variant from **e** at their brightest states (image size: 775 μm × 775 μm). **g**, Quantitative emission spectra (starting from their respective emission maxima) for each sensor normalized to photon counts from its fused eGFP (red, HyperRed; magenta, oROS-HT$_{635}$; sky blue inset, magnified HyPerRed–eGFP spectra; $n > 100$ cells each from 3 wells). Dashed lines denote the half-width at half-maximum of oROS-HT$_{635}$ and HyperRed spectra from which we approximated their full-width at half-maximum (FWHM). **h**, Expression of oROS-HT$_{635}$ in primary cortical neurons (primary-CN), ex vivo rat cortex (brain slice) and hiPS cell-derived cortical neurons (hiPS cell-CN) and their responses to exogenous 300 μM H_2O_2; scale bars, 100 μm. Error bars and bands in the plots represent the 95% bootstrap ($n = 1{,}000$) CI of the mean calculated using the statistical plotting package Seaborn (v0.13.2).

features of oROS-HT$_{635}$ that demonstrate its environmental resiliency. ecOxyR-based H_2O_2 sensors have been shown to possess superior specificity toward H_2O_2 compared to chemical H_2O_2 tracers[15,20,49]. This specificity stems from its unique hydrogen bond network in the ligand binding pocket network that induces H_2O_2-specific disulfide linkage between two highly conserved cysteine residues (ecOxyR-regulatory domain C199–C208). Consistent with previous reports, disabling disulfide formation by a C199S mutation eliminates H_2O_2-induced fluorescence (loss of function), demonstrating that oROS-HT$_{635}$ responses are H_2O_2 specific. Nevertheless, fluorescence is intrinsically prone to environmental artifacts, including pH change, absorption and interference from autofluorescence. As a negative control, oROS-HT$_{635}$-C199S can reflect environmental effects on the fluorescent signals not generated by H_2O_2 sensing[15] (Supplementary Fig. 7). oROS-HT$_{635}$ exhibited improved resiliency to environmental factors (for example, pH, photoartifacts, aggregation and oxygen) compared to the red fluorescent H_2O_2 sensor HyPerRed. We observed pH-dependent fluorescence changes in extracellular oROS-HT$_{635}$ (Fig. 3a). However, a comparison between intracellular oROS-HT$_{635}$ and HyperRed demonstrated a noticeably improved pH resilience in oROS-HT$_{635}$ (Fig. 3b). Red-shifted GEHIs are often limited for polychromatic use with green sensors due to a photochromic false-positive artifact in response to blue light[50]. oROS-HT$_{635}$ lacks this artifact, rendering oROS-HT$_{635}$ more compatible with green reporters (Fig. 3c). To demonstrate its dual-color imaging capabilities, we coexpressed oROS-HT$_{635}$ or oROS-HT$_{635}$-C199S with the GFP-based pH indicator SypHer3s to simultaneously image H_2O_2 and pH changes. Extracellular pH insults (pH 6 and 9) resulted in corresponding cytosolic changes, as confirmed by SypHer3s responses, whereas the fluorescence of oROS-HT$_{635}$-C199S was not affected (Fig. 3d). We next tested whether oROS-HT$_{635}$ maintains function under an acidic pH insult (pH 6). oROS-HT$_{635}$ did not respond to the initial change in pH, as confirmed by SypHer3s responses, but a menadione-induced increase

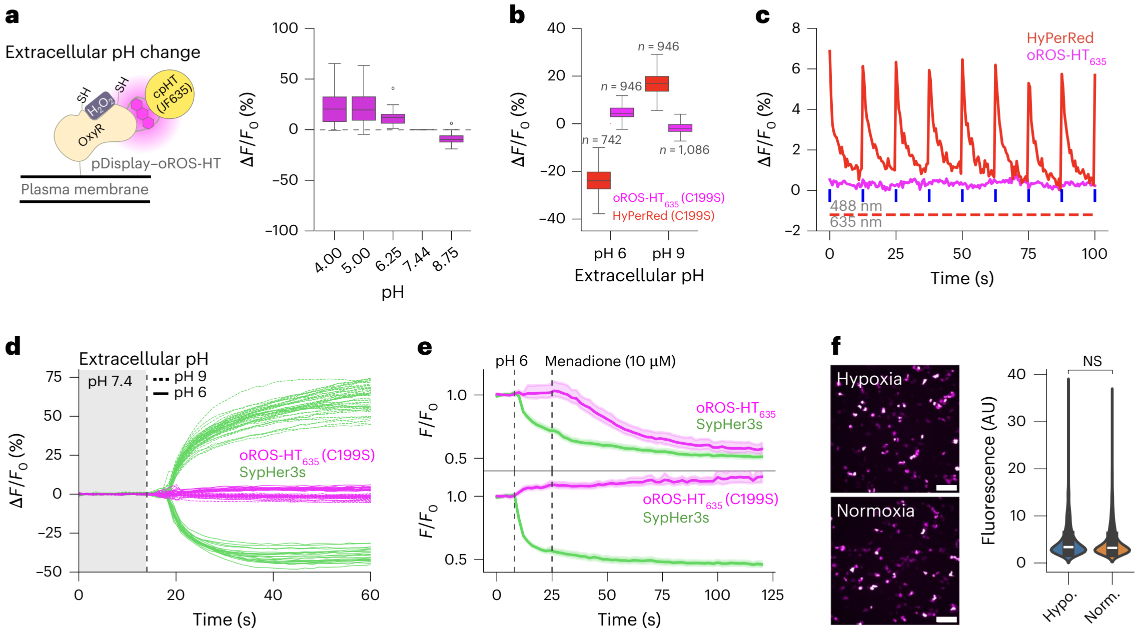

Fig. 3 | Biophysical properties and versatility of oROS-HT$_{635}$ under varying environmental conditions. a, pDisplay–oROS-HT$_{635}$ was used for extracellular expression of oROS-HT$_{635}$, and fluorescence was measured under various pH conditions using different media formulations. Fluorescence intensities were normalized to the intensity at pH 7.44 (indicated by the dotted line), which served as the baseline (*n* = 36 cells from three wells). **b**, $\Delta F/F_0$ (%) of cytosolic oROS-HT$_{635}$-C199S (loss of function) and cytosolic HyPerRed-C199S expressed in HEK293 cells exposed to an extracellular pH of 9 or 6. **c**, Representative fluorescence emission of oROS-HT$_{635}$ and HyPerRed under their respective excitation wavelengths (635 nm and 597 nm) and in response to 488-nm light pulses. **d**, Multiplexed imaging of oROS-HT$_{635}$-C199S and the green fluorescent pH sensor SypHer3s coexpressed in HEK293 cells. Neutral imaging solution (pH 7.44) was switched to either an acidic (pH 6, *n* = 22 cells) or basic (pH 9, *n* = 47 cells) imaging solution at the vertical dashed line (gray). **e**, Dual monitoring of pH and H_2O_2 in HEK293 cells. Either oROS-HT$_{635}$ or oROS-HT$_{635}$-C199S was paired with SypHer3s, a green fluorescent pH indicator that monitors (1) pH environment change (pH 6) and (2) menadione (10 μM)-induced H_2O_2 increase (*n* > 100 cells per condition from 3 wells). **f**, Maturation of oROS-HT$_{635}$-C199S under hypoxic conditions. HEK293 cells expressing loss-of-function oROS-HT$_{635}$-C199S were incubated under either normoxia (Norm.; atmospheric conditions at 37 °C) or hypoxia (Hypo.; N_2-infused chamber at 37 °C) overnight (18 h). Left: representative images of oROS-HT$_{635}$-C199S maturated in HEK293 cells under hypoxic or normoxic conditions; scale bars, 100 μm. Right: fluorescence intensity profile of oROS-HT$_{635}$-C199S (hypoxia (*n* = 1,246 cells) and normoxia (*n* = 1,765 cells) collected from 8 or 11 wells, respectively). Error bars and bands in the plots represent the 95% bootstrap (*n* = 1,000) CI of the mean calculated using the statistical plotting package Seaborn (v0.13.2). Box plots show the median, interquartile range (IQR), whiskers (extending to 1.5× IQR) and outliers. Data were analyzed by two-sided independent *t*-test in **f**; NS, not significant; AU, arbitrary units.

in cytosolic H_2O_2 was still detected (Fig. 3e), exemplifying robust functionality under changing cellular pH environments. Most β-barrel FPs in sensor designs require oxygen for their fluorophore maturation[51,52]. In addition, GFP undergoes photoconversion under hypoxic conditions, where the excitation/emission spectra shift and become similar to RFP[53]. By contrast, HaloTag-rhodamine-based chemigenetic sensors incorporate synthetic fluorophores, which do not require oxygen for fluorescence. HEK293 cells transfected with oROS-HT$_{635}$-C199S showed no significant differences in fluorescence under normoxic or hypoxic conditions (Fig. 3f).

Acute effect of auranofin on H_2O_2 and glutathione redox potential in HEK cells

GRX1–roGFP2 is an indicator sensitive to glutathione redox potential (E_{GSH}) and is a fusion between glutaredoxin1 (GRX1) and the redox-sensitive GFP roGFP2. Multiplexed imaging of oROS-HT$_{635}$ with GRX1–roGFP2 could enable H_2O_2 imaging with augmented information about the redox cellular environment. Here, we monitored both sensors simultaneously in HEK293 cells following exposure to 10 μM H_2O_2. We demonstrated sequential events of increases in intracellular H_2O_2, followed by a decrease in E_{GSH} (peak$_{oROS\text{-}HT635}$ to peak$_{GRX1}$ = 3.12 s; Fig. 4a). By contrast, the reduction of cellular antioxidative capacity using the selective thioredoxin reductase and glutathione peroxidase inhibitor auranofin (1 μM) showed a rapid decrease in E_{GSH}, followed by a slow increase in intracellular H_2O_2. Interestingly, the auranofin-induced H_2O_2 buildup was transient (Fig. 4b). The reversal of H_2O_2 levels could be triggered by increased stress-induced antioxidative responses. We observed increased translocation of NRF2 into the nucleus in HEK293 cells within 30 min of exposure to 1 μM auranofin (Fig. 4c and Supplementary Fig. 8). The translocation of NRF2 is a hallmark of rapid cellular antioxidative responses, consistent with previous findings[54,55]. In agreement with our results, they confirmed fast NRF2 nuclear translocation within 10 min to 1 h. We therefore conclude that NRF2 triggered an antioxidant cellular response and subsequently reversed the pharmaceutically induced increase in H_2O_2 levels. The multiplexed use of GRX1–roGFP2 with oROS-HT$_{635}$ established a temporal and spatial correlation between H_2O_2 levels and the cellular redox environment.

H_2O_2 and Ca^{2+} transients in hiPS cell-CMs

Although there is growing evidence of a mutual interplay between redox and Ca^{2+} dynamics in biological systems[56], existing molecular imaging tools are limited to asynchronous studies of Ca^{2+} and H_2O_2 in biological systems. However, simultaneous measurements would provide a distinct advantage in establishing a better temporal and spatial correlation between these two biological phenomena. Polychromatic measurements of H_2O_2 with oROS-HT$_{635}$ could enable simultaneous real-time observations of oxidative stress and Ca^{2+} in the same cell with a temporal resolution that can capture dynamic Ca^{2+} transients (CaTs). Here, we performed dual-color imaging of H_2O_2 and CaTs using oROS-HT$_{635}$ with Fluo-4, a Ca^{2+}-sensitive green fluorescent dye in hiPS cell-CMs (Fig. 4d). It is is widely accepted that oxidative stress perturbs key Ca^{2+} transporters like ryanodine receptors (sarcoplasmic reticulum

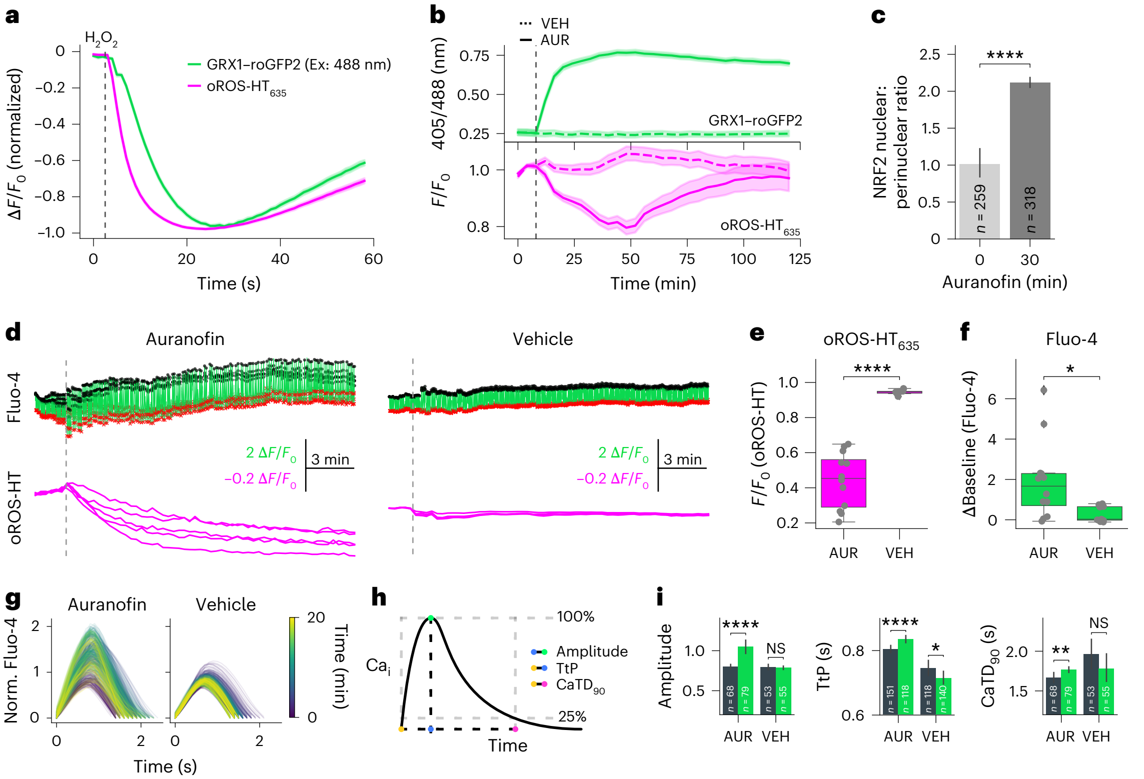

Fig. 4 | Multiparametric analysis of the acute effect of auranofin on H_2O_2, redox potential and Ca^{2+}. **a**–**c**, Dual monitoring of intracellular E_{GSH} and H_2O_2. **a**, Normalized fluorescence change in GRX1–roGFP2 (green, E_{GSH} sensor) and oROS-HT_{635} (magenta) coexpressed in HEK293 cells in response to 10 µM H_2O_2 (at the gray line, $n > 100$ cells, collected from 3 wells). Ex, excitation. **b**, Traces of auranofin-induced changes in GRX1–roGFP2 and oROS-HT_{635} in HEK293 cells. oROS-HT_{635} response (magenta) is shown as relative fluorescence change from the baseline (F/F_0). GRX1-roGFP2 response (green) is shown as intensity ratio from 405/488 (nm) excitation. The dashed trace for each sensor plot represents responses to vehicle treatment ($n > 100$ cells per condition collected from 3 wells); AUR, auranofin; VEH, vehicle. **c**, Translocation of NRF2 (in nuclear:perinuclear ratio) quantified from immunofluorescence staining of NRF2 in HEK293 cells exposed to 1 µM auranofin for 30 min or negative controls ($n > 100$ cells collected from 5 wells per condition). Detailed analysis methods are described in Supplementary Fig. 8. **d**–**i**, Dual imaging of Ca^{2+} and H_2O_2 in hiPS cell-CMs in response to 5 µM auranofin ($n = 12$ for auranofin and $n = 11$ for vehicle conditions; regions of interest from 3 wells), **d**, Representative traces. Peaks (black dots) and troughs (red crosses) of CaTs are labeled. **e**, Fluorescence change (F/F_0) of oROS-HT_{635}. **f**, Resting fluorescence change (ΔBaseline) of Fluo-4. **g**, Representative CaT changes over time. **h**, Schematic description of CaT phenotypes; Ca_i, intracellular Ca^{2+}. **i**, Extracted CaT phenotypes. Left: amplitude (amplitude of CaTs at the peak). Middle: TtP, time-to-peak. Right: $CaTD_{90}$. Error bars and bands in the plots represent the 95% bootstrap ($n = 1{,}000$) CI of the mean calculated using the statistical plotting package Seaborn (v0.13.2). Box plots show median, IQR, whiskers (extending to 1.5× IQR) and outliers. Data in **c**, **e**, **f** and **i** were analyzed by two-sided independent t-test; $^{*}P < 0.05$, $^{**}P < 0.01$ and $^{****}P < 0.0001$.

(SR) Ca^{2+} leak)[57], L-type Ca^{2+} channels (I_{CaL}; inward Ca^{2+} current)[58] and SR Ca^{2+} ATPase pumps (SERCA; decreased Ca^{2+} reuptake)[59–61]. Physiological effects of these perturbations can include changes in specific CaT phenotypes, such as baseline Ca^{2+} levels, CaT amplitudes, time to peak (TtP; on-kinetics) and Ca^{2+} transient duration 90% ($CaTD_{90}$; completion of 90% of one CaT period). We tested how auranofin-induced acute oxidative stress perturbs Ca^{2+} dynamics. Previous studies reported auranofin-induced Ca^{2+} increases in some cell types[62,63]. Indeed, auranofin (5 µM) induced increased H_2O_2 (Fig. 4e) during the 20-min imaging period, accompanied by an increase in basal Ca^{2+} levels (Fig. 4f). Next, we extracted the CaT profiles from the Fluo-4 imaging data for further characterization (Fig. 4g,h). Compared to the vehicle control, CaTs of auranofin-treated hiPS cell-CMs exhibited the following phenotypes: elevated CaT peak amplitude and prolonged TtP and $CaTD_{90}$ (Fig. 4i).

Modeling the impact of oxidative stress on CaTs of hiPS cell-CMs

Here, we used a previously described 'generalized' computational model[64] for hiPS cell-CM electrophysiology to explore mechanisms of how oxidative stress leads to the observed CaT phenotypes (that is, increased amplitude, TtP and $CaTD_{90}$). Aligned with the reported effect of oxidative stress on the Ca^{2+} transporters discussed earlier, we modeled oxidative stress by modifying parameters corresponding to Ca^{2+} uptake from the cytoplasm to the SR via SERCA, SR Ca^{2+} leak amplitude and I_{CaL} conductance. Perturbing SR Ca^{2+} leak did not alter CaT profiles, while modifying I_{CaL} and SERCA levels elicited changes in CaT (Fig. 5a–c). We thus performed a bivariate analysis to determine how CaT phenotype depended on SERCA and I_{CaL} levels. This revealed that CaT phenotypes aligned with experimental observations only emerged when synergistic perturbations were modeled (Fig. 5d). CaT profiles were generally more sensitive to changes in I_{CaL} than SERCA (Fig. 5e), consistent with previous reports identifying I_{CaL} as the primary CaT driver in hiPS cell-CMs due to the functional immaturity of SR-associated Ca^{2+} transporters[65–69]. However, steady-state beating frequencies from the modeled perturbations ranged from 0.479 to 0.846 Hz, with a trend toward faster activity, aligning with experimental findings where auranofin increased frequency in two of three replicates (Supplementary Fig. 9a). To verify that observed changes in CaT phenotypes stemmed from parameter modifications rather than changes in intrinsic beating rate, we ran additional simulations (Supplementary Fig. 9b) by overdrive pacing the baseline model (0.5 Hz) up to 0.85 Hz. This resulted only in minor or opposite changes in CaT metrics (CaT amplitude decreased with pacing but increased under modifications simulating oxidative stress). Thus, although the CaT phenotypes in hiPS cell-CMs are more responsive to changes in

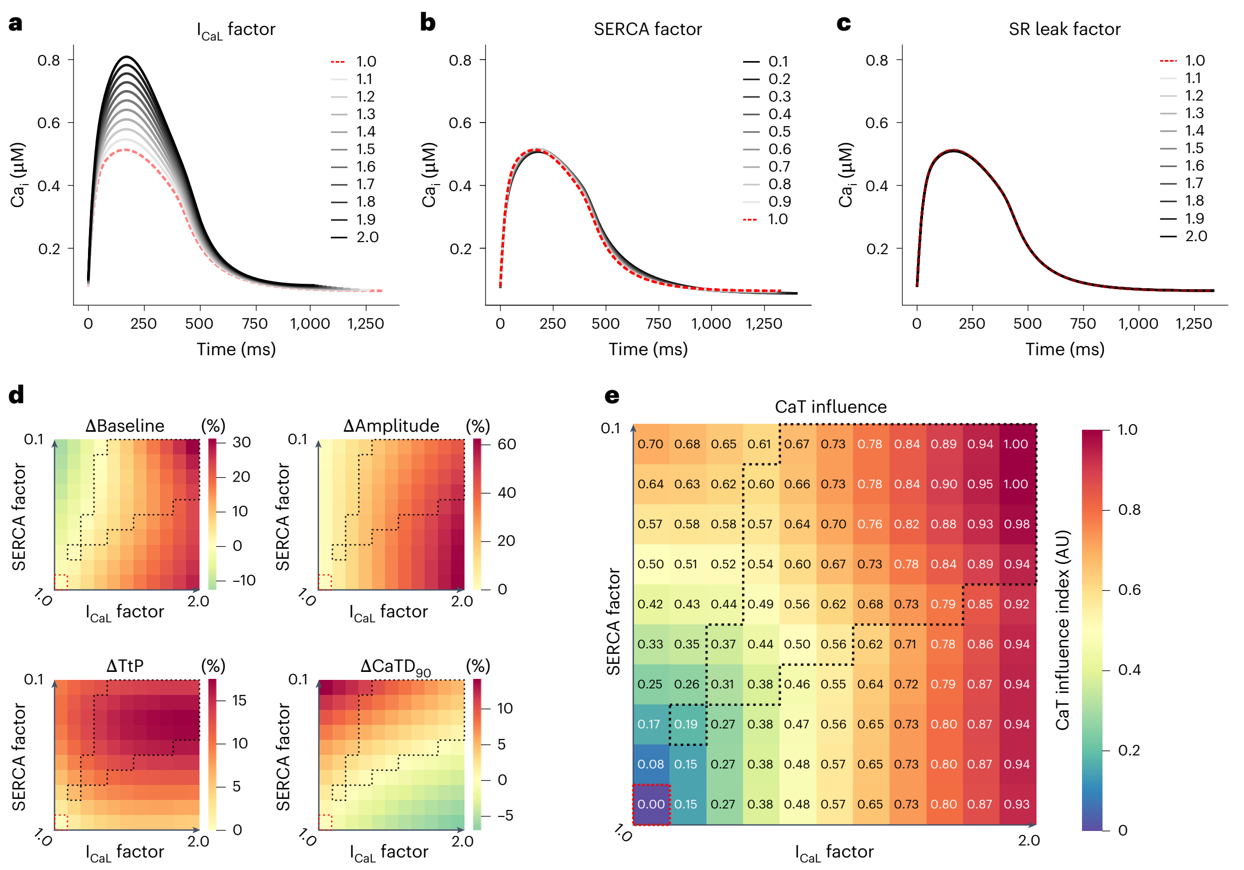

Fig. 5 | Modeled interplay between I_{CaL} and SERCA reveals oxidative stress-induced Ca^{2+} dysregulation. a–c, Effects of oxidative stress-induced perturbation on I_{CaL} conductance (**a**), SERCA uptake (**b**) and SR Ca^{2+} leak (**c**) were simulated using a modified version of the hiPS cell-CM computational model by Kernik et al.[64] (total simulation time = 100 s, with baseline beating frequency of 0.5 Hz calibrated to match the experimental data). The plots display cytoplasmic CaTs at steady state from each simulated condition. Red dashed lines represent simulations without perturbation. **d**, Synergy map showing the degree of difference in CaT phenotypes in each simulated condition compared to conditions with no perturbation (Δphenotype/$\text{phenotype}_{1.0}$). $\text{Phenotype}_{1.0}$ is within the red dotted boundary. The grid boxes within the black dotted boundary denote conditions whose direction of phenotypic change (+ or −) matches the CaT phenotypes (ΔBaseline, ΔAmplitude, ΔTtP and $ΔCaTD_{90}$) observed in Fig. 4d–i. **e**, CaT influence map (I_{CaL} versus SERCA) derived from an additive weighting of absolute influence on each phenotype (|Δphenotype/$\text{phenotype}_{1.0}$| from ΔBaseline, ΔAmplitude, ΔTtP and $ΔCaTD_{90}$). Synergistic perturbation of both I_{CaL} and SERCA was sufficient to recapitulate the experimentally observed CaT phenotypes.

I_{CaL}, the experimentally observed CaT profiles only arise when both plasma membrane and SR components are synergistically perturbed. In other words, perturbations of both I_{CaL} and SERCA were sufficient to recapitulate the observed phenotypes. These results highlight the complex nature of the effect of oxidative stress on Ca^{2+} dynamics in cardiomyocytes, further emphasizing the need for systemic studies on the influence of oxidative stress on specific Ca^{2+} transporters and their synergistic interactions.

Imaging intracellular and extracellular H_2O_2 induced by menadione

Intracellular H_2O_2 generation is potentially localized and functionally differentiated in aerobic organisms[70], which calls for monitoring of H_2O_2 in a spatially resolved manner[20] (for example, in subcellular compartments; Fig. 6a and Supplementary Fig. 10). Growing evidence demonstrates the substantial contribution of NADPH oxidase-sourced O_2^- and H_2O_2 in redox signaling and disease progression[71–75]. The oxidase generates H_2O_2 on the extracellular side of the cellular plasma membrane[76], constituting an extracellular pool of H_2O_2 (ref. 77). Furthermore, its intracellular distribution is achieved through autocrine (aquaporin-mediated diffusion of H_2O_2 (refs. 78,79) into cells) and paracrine[80] mechanisms. We fused oROS-HT_{635} to a PDGFR transmembrane domain-based trafficking sequence (pDisplay vector; Invitrogen) for extracellular membrane localization. Its coexpression with oROS-G, a sensitive and equivalently fast green variant of oROS that we previously engineered[30], was well tolerated in HEK293 cells (Fig. 6b). We measured increases in H_2O_2 in both the extracellular and intracellular space following application of 25 μM menadione. Intriguingly, we found that the extracellular H_2O_2 response detected by oROS-HT_{635} (inverse response sensor) was faster than oROS-G (direct response sensor) in cells where both sensors responded to menadione. This supports previous observations that menadione increases H_2O_2 in the extracellular space, potentially via NADPH oxidase-sourced H_2O_2 (refs. 81–84; Fig. 6c,d).

Monitoring spatially controlled H_2O_2 diffusion

We visualized spatiotemporally resolved diffusion of H_2O_2 by combining subcellular variants of oROS-HT_{635} with compartment-specific chemogenetic and optogenetic H_2O_2-generating methods. We first targeted D-amino acid oxidase (DAAO)[14] to the mitochondrial matrix (dMito-DAAO), which generated H_2O_2 in response to D-alanine (50 mM) supplementation. H_2O_2 generated in the matrix was tracked in different compartments using subcellular oROS-HT_{635} at the source (dMito), the intermembrane space (IMS) and the inner plasma membrane (via CAAX sequence). As expected, the sensors captured the time course of H_2O_2 diffusion from the mitochondria to the inner plasma membrane (5–95% $\Delta F/F_0$ (min ± s.d.): dMito (1.89 ± 0.21), IMS (3.86 ± 0.60) and CAAX (7.81 ± 0.39)), thereby revealing buffering along the path

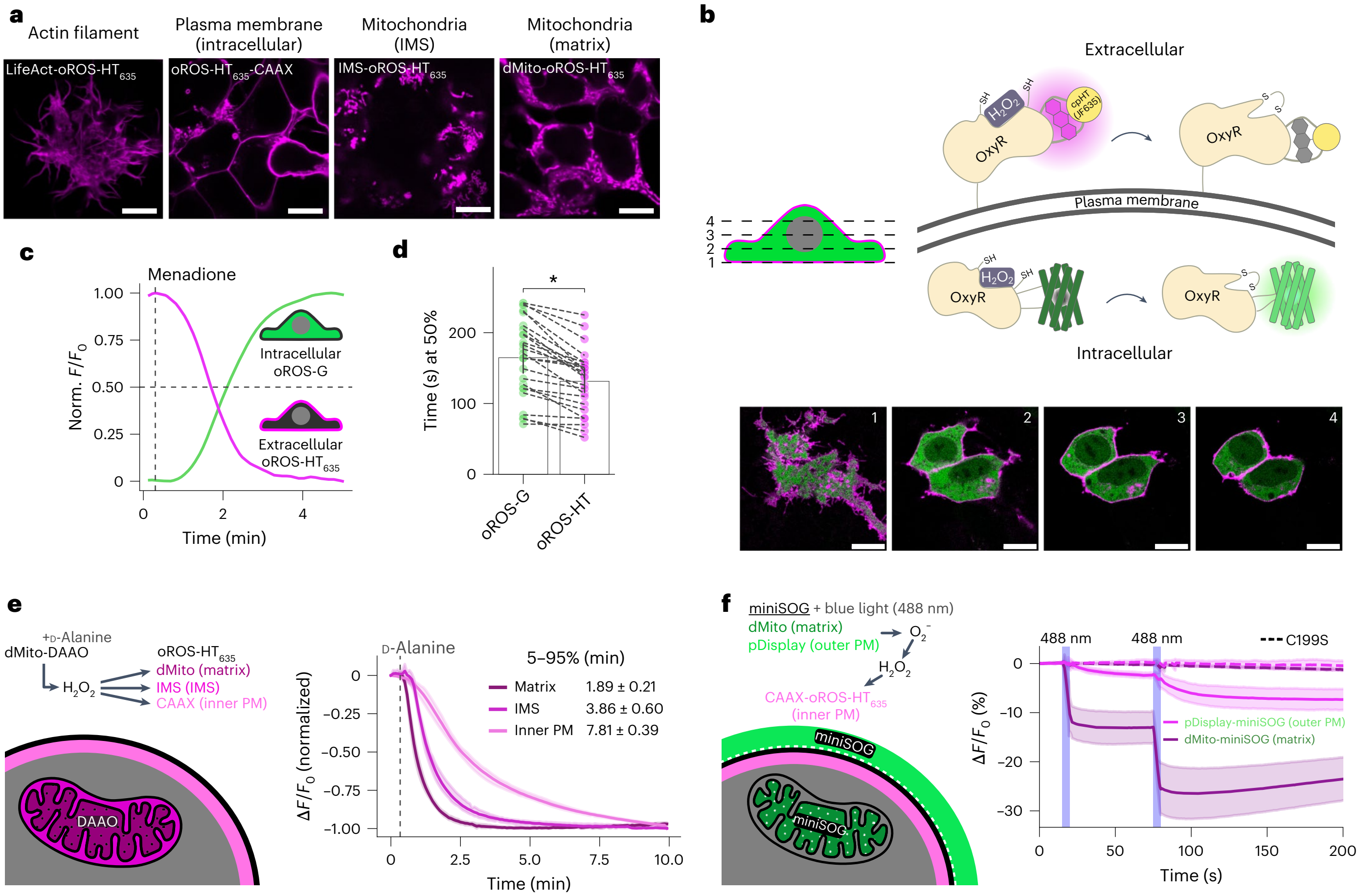

Fig. 6 | Spatiotemporally resolved imaging of H_2O_2. **a**, Subcellular localization of oROS-HT_{635} was achieved by labeling peptide sequences for actin (LifeAct), mitochondrial matrix (dMito), mitochondrial IMS and the intracellular side of the plasma membrane (CAAX). HEK293 cells expressing each trafficking variant were live imaged using a confocal microscope; scale bars, 10 µm. **b**, Schematic and confocal *z*-stack images of HEK293 cells coexpressing pDisplay–oROS-HT_{635} (extracellular side of the plasma membrane) and cytosolic oROS-G; scale bars, 10 µm. **c**,**d**, Change in fluorescence in HEK293 cells expressing pDisplay–oROS-HT_{635} and cytosolic oROS-G in response to 25 µM menadione imaged with an epifluorescence microscope. Both sensors were imaged every second. **c**, Representative trace of oROS-HT_{635} and oROS-G from a single cell. **d**, Time (s) at 50% sensor activation ($n = 25$ cells from 4 biological replicates). **e**, Activation kinetics of chemogenetically induced mitochondrial H_2O_2 to the mitochondrial matrix (matrix), IMS and inner plasma membrane (inner PM; 3 biological replicates, ±s.d. for 5–95% time). **f**, miniSOG generated O_2^- and H_2O_2 following 488-nm stimulation and was expressed at the outer plasma membrane or the mitochondrial matrix. CAAX-oROS-HT measured optogenetically induced H_2O_2 diffusion to the inner plasma membrane (three biological replicates). Error bars and bands in the plots represent the 95% bootstrap ($n = 1{,}000$) CI of the mean calculated using the statistical plotting package Seaborn (v0.13.2). Data in **d** were analyzed by two-sided independent *t*-test; $^*P < 0.05$.

exemplified by the longer temporal delay of diffusion from the IMS to the inner plasma membrane than from the matrix to the IMS (Fig. 6e). In addition, mitochondrial H_2O_2 from dMito-DAAO diffused outside of cells. We detected this paracrine diffusion of H_2O_2 in cocultures of dMito-DAAO$^+$ cells expressing cytosolic oROS-G (50% activation at ~20.3 min) and dMito-DAAO$^-$ cells expressing cytosolic oROS-HT_{635} (50% activation at ~36.5 min; Supplementary Fig. 11). Furthermore, we used the photosensitizer miniSOG, which produces singlet oxygen and O_2^- following 488-nm excitation and subsequently dismutates to H_2O_2 via physiological mechanisms such as superoxide dismutase[85,86]. By targeting miniSOG to two major endogenous H_2O_2 sources (the mitochondrial matrix (via dMito) and the outer plasma membrane (via pDisplay)), we assessed H_2O_2 diffusion toward the inner plasma membrane using CAAX-oROS-HT_{635}. Both mitochondrial and outer plasma membrane miniSOG induced detectable increases in H_2O_2 at the inner plasma membrane. However, the mitochondrial matrix miniSOG produced a faster and more substantial response (first 488-nm pulse, minimum $\Delta F/F_0$ (%) ± s.d.: pDisplay −2.46 ± 0.55 and dMito −13.19 ± 3.34; second 488-nm pulse, minimum $\Delta F/F_0$ (%): pDisplay −7.38 ± 2.14 and dMito −26.52 ± 5.17; Fig. 6f). Combining dual-color H_2O_2 imaging and plasma membrane-specific expression of oROS-HT_{635}, as demonstrated here, could aid in the study of interactions between H_2O_2 sources and intracellular and extracellular targets with subcellular resolution.

Discussion

This study introduces a bright far-red chemigenetic indicator for H_2O_2, oROS-HT_{635}. To fully exploit the brightness of the JF635 rhodamine dye, we optimized the inverted-response sensor for higher brightness and dynamic range. Because oROS-HT_{635} maintains bright fluorescence in the sensor activation range (for example, partially oxidized state), it detects high-fidelity signals at physiological H_2O_2 levels (Fig. 2g). By incorporating a chemigenetic reporter system (cpHaloTag-JF635), we achieved oxygen-insensitive, pH-resistant and photochromic artifact-free imaging, extending its application range (Fig. 3).

Harnessing the multiplexing capability of oROS-HT_{635}, we performed dual-color imaging paired with green fluorescence-based redox potential, Ca^{2+} and pH reporters, allowing monitoring of H_2O_2 levels simultaneously with changes in redox potential, Ca^{2+} or pH (Figs. 3d,e and 4). Auranofin, a treatment for rheumatoid arthritis, is gaining attention from the cancer community as a potential therapeutic candidate due to its dose- and cell-dependent multifaceted mode of action[87,88]. As a thioredoxin reductase/glutathione peroxidase inhibitor, auranofin attenuates intracellular antioxidant capacity, which increases oxidative stress. Intriguingly, recent studies aimed to repurpose auranofin as a potential cancer therapeutic revealed a more nuanced role of auranofin as increasing cellular oxidative stress can activate regulators such as NRF2 to boost cellular antioxidative capacity[87,88]. Here, we showed in real time how low-dose auranofin initiates transient oxidative stress, followed by a GRX-independent reversal of H_2O_2 levels. The time course of the reversal correlated with increased NRF2 translocation into the cell nucleus in HEK293 cells, supporting observations from previous studies (Fig. 4b,c).

Auranofin-induced antioxidative perturbations also altered dynamic CaTs in hiPS cell-CMs, which we correlated with an increased level of H_2O_2. These observations could be recapitulated in our computational simulation of the effect of oxidative stress on two key Ca^{2+} transporters I_{CaL} and SERCA[56,57,61] (Figs. 4d–i and 5). Our findings align with previous work showing a close link between oxidative stress and Ca^{2+} transport across various cell types. We want to acknowledge the intricate nature of Ca^{2+} and redox interactions, which may become more pronounced in fully developed cardiomyocytes. This study focused on I_{CaL} and SERCA changes to replicate the observed responses in hiPS cell-CMs. However, in mature heart cells, factors like cardiac dyad structure, mitochondrial function and NCX activity may amplify the effects of reactive oxygen species on Ca^{2+} dynamics. These complexities require further exploration of how these interactions evolve with cellular development to better understand the roles of oxidative stress in Ca^{2+} handling across diverse cell types and developmental stages.

Users can also exploit the remarkable subcellular targeting of oROS-HT_{635} to monitor H_2O_2 with higher spatial resolution closer to or farther from its sources. GEHIs have been pivotal in unraveling cellular H_2O_2 topology by enabling optical monitoring of H_2O_2 dynamics in a spatially resolved manner heavily focused on cytoplasmic and mitochondrial spaces[14,89]. oROS-HT_{635} can aid users in studying H_2O_2 biology by revealing the H_2O_2 dynamics near plasma membrane spaces[72,90,91] and paracrine H_2O_2 (ref. 80), allowing a more nuanced and systemic understanding of H_2O_2 dynamics in biological systems. Specifically, membrane-tagged oROS-HT_{635} provides opportunities to investigate H_2O_2 topology proximal to the plasma membrane[81–84] (Fig. 6).

The JF635-based design of oROS-HT_{635} led to critical advantages such as bright far-red fluorescence, oxygen independence and reduced pH dependence. Because the dye covalently conjugates with the sensor, the fluorescence is not dependent on free dye concentration once the conjugation occurs. However, dependency on the exogenous dye creates a potential disadvantage of oROS-HT_{635} over existing cpFP-based H_2O_2 sensors. The oROS-HT_{635} readout in this publication relies on intensiometric measurements, which makes signals inherently qualitative. Nevertheless, the sensor provides precise temporal and spatial correlations between H_2O_2-generating events and subsequent physiological phenomena. For steady-state measurements, different sensor expression levels must be accounted for, for example, by including a control fluorophore.

The next iteration of oROS-HT_{635} could be optimized for other JF dyes with shifted emission spectra ranging from 494 nm to 722 nm, further enhancing its flexibility in multiplexed optogenetic applications. Another possible avenue for future oROS-HT_{635} development is maximizing its in vivo application capability. As a trade-off to its exceptional fluorogenicity, the bioavailability of JF635 dye can be a challenge for animal application in vivo. We envision two paths for optimizing the use of oROS-HT_{635} in live animals. First, introducing the dye into brain tissue can be aided by engineered solutions such as injection cannulas or drug delivery systems[92,93]. Alternatively, as recently described by Farrants et al., optimization of oROS-HT_{635} with highly bioavailable dyes (for example, JF669)[94,95] can be explored for efficient animal applications. Adapting the sensor's reporting mechanism to be more prone to quantum yield change could also improve fluorescence lifetime imaging microscopy compatibility for more quantitative measurement of H_2O_2 in situ.

In conclusion, oROS-HT_{635} enables the monitoring of H_2O_2 with high spatiotemporal resolution, offering flexibility in its multiplexed application with existing optogenetic tools. The rapid kinetics and robust subcellular targeting capabilities of oROS-HT_{635}, particularly at the outer and inner surfaces of the plasma membrane, render it an invaluable tool for investigating H_2O_2 topology near the plasma membrane. When used with fluorescent sensors for various analytes, oROS-HT_{635} facilitates a dynamic, multiparametric analysis of H_2O_2 dynamics and physiological responses in real time with precise spatial information, enhancing the contextual understanding of H_2O_2 in cell physiology.

Online content

Any methods, additional references, Nature Portfolio reporting summaries, source data, extended data, supplementary information, acknowledgements, peer review information; details of author contributions and competing interests; and statements of data and code availability are available at https://doi.org/10.1038/s41589-025-01891-7.

References

1. Forman, H. J. & Zhang, H. Targeting oxidative stress in disease: promise and limitations of antioxidant therapy. *Nat. Rev. Drug Discov.* **20**, 689–709 (2021).
2. Sies, H. & Jones, D. P. Reactive oxygen species (ROS) as pleiotropic physiological signalling agents. *Nat. Rev. Mol. Cell Biol.* **21**, 363–383 (2020).
3. Sies, H. Hydrogen peroxide as a central redox signaling molecule in physiological oxidative stress: oxidative eustress. *Redox Biol.* **11**, 613–619 (2017).
4. Schieber, M. & Chandel, N. S. ROS function in redox signaling and oxidative stress. *Curr. Biol.* **24**, R453–R462 (2014).
5. Finkel, T. Signal transduction by reactive oxygen species. *J. Cell Biol.* **194**, 7–15 (2011).
6. D'Autréaux, B. & Toledano, M. B. ROS as signalling molecules: mechanisms that generate specificity in ROS homeostasis. *Nat. Rev. Mol. Cell Biol.* **8**, 813–824 (2007).
7. Ren, X. et al. Redox signaling mediated by thioredoxin and glutathione systems in the central nervous system. *Antioxid. Redox Signal.* **27**, 989–1010 (2017).
8. Marinho, H. S., Real, C., Cyrne, L., Soares, H. & Antunes, F. Hydrogen peroxide sensing, signaling and regulation of transcription factors. *Redox Biol.* **2**, 535–562 (2014).
9. Johnson, F. & Giulivi, C. Superoxide dismutases and their impact upon human health. *Mol. Aspects Med.* **26**, 340–352 (2005).
10. Martin, C., Binda, C., Fraaije, M. W. & Mattevi, A. The multipurpose family of flavoprotein oxidases. *Enzymes* **47**, 63–86 (2020).
11. Halliwell, B. Understanding mechanisms of antioxidant action in health and disease. *Nat. Rev. Mol. Cell Biol.* **25**, 13–33 (2024).
12. Kishi, S., Nagasu, H., Kidokoro, K. & Kashihara, N. Oxidative stress and the role of redox signalling in chronic kidney disease. *Nat. Rev. Nephrol.* **20**, 101–119 (2024).
13. Chun, H. et al. Severe reactive astrocytes precipitate pathological hallmarks of Alzheimer's disease via $H_2O_2^-$ production. *Nat. Neurosci.* **23**, 1555–1566 (2020).
14. Pak, V. V. et al. Ultrasensitive genetically encoded indicator for hydrogen peroxide identifies roles for the oxidant in cell migration and mitochondrial function. *Cell Metab.* **31**, 642–653 (2020).
15. Ermakova, Y. G. et al. Red fluorescent genetically encoded indicator for intracellular hydrogen peroxide. *Nat. Commun.* **5**, 5222 (2014).
16. Pang, Y. et al. SHRIMP: genetically encoded mScarlet-derived red fluorescent hydrogen peroxide sensor with high brightness and minimal photoactivation. Preprint at *bioRxiv* https://doi.org/10.1101/2023.08.09.552302 (2023).

17. Morgan, B. et al. Real-time monitoring of basal H_2O_2 levels with peroxiredoxin-based probes. *Nat. Chem. Biol.* **12**, 437–443 (2016).
18. Gutscher, M. et al. Proximity-based protein thiol oxidation by H_2O_2-scavenging peroxidases. *J. Biol. Chem.* **284**, 31532–31540 (2009).
19. Eid, M., Barayeu, U., Sulková, K., Aranda-Vallejo, C. & Dick, T. P. Using the heme peroxidase APEX2 to probe intracellular H_2O_2 flux and diffusion. *Nat. Commun.* **15**, 1239 (2024).
20. Murphy, M. P. et al. Guidelines for measuring reactive oxygen species and oxidative damage in cells and in vivo. *Nat. Metab.* **4**, 651–662 (2022).
21. Patriarchi, T. et al. An expanded palette of dopamine sensors for multiplex imaging in vivo. *Nat. Methods* **17**, 1147–1155 (2020).
22. Dana, H. et al. Sensitive red protein calcium indicators for imaging neural activity. *eLife* **5**, e12727 (2016).
23. Wu, J. et al. Improved orange and red Ca^{2+} indicators and photophysical considerations for optogenetic applications. *ACS Chem. Neurosci.* **4**, 963–972 (2013).
24. Ning, L. et al. A bright, nontoxic, and non-aggregating red fluorescent protein for long-term labeling of fine structures in neurons. *Front. Cell Dev. Biol.* **10**, 893468 (2022).
25. Pedre, B. et al. Structural snapshots of OxyR reveal the peroxidatic mechanism of H_2O_2 sensing. *Proc. Natl Acad. Sci. USA* **115**, E11623–E11632 (2018).
26. Åslund, F., Zheng, M., Beckwith, J. & Storz, G. Regulation of the OxyR transcription factor by hydrogen peroxide and the cellular thiol-disulfide status. *Proc. Natl Acad. Sci. USA* **96**, 6161–6165 (1999).
27. Tao, K. In vivo oxidation–reduction kinetics of OxyR, the transcriptional activator for an oxidative stress-inducible regulon in *Escherichia coli*. *FEBS Lett.* **457**, 90–92 (1999).
28. Lee, C. et al. Redox regulation of OxyR requires specific disulfide bond formation involving a rapid kinetic reaction path. *Nat. Struct. Mol. Biol.* **11**, 1179–1185 (2004).
29. Mirdita, M. et al. ColabFold: making protein folding accessible to all. *Nat. Methods* **19**, 679–682 (2022).
30. Lee, J. D. et al. Structure-guided engineering of a fast genetically encoded sensor for real-time H_2O_2 monitoring. Preprint at *bioRxiv* https://doi.org/10.1101/2024.01.31.578117 (2024).
31. Choi, H. et al. Structural basis of the redox switch in the OxyR transcription factor. *Cell* **105**, 103–113 (2001).
32. Jo, I. et al. Structural details of the OxyR peroxide-sensing mechanism. *Proc. Natl Acad. Sci. USA* **112**, 6443–6448 (2015).
33. Fenno, L. E. et al. Comprehensive dual- and triple-feature intersectional single-vector delivery of diverse functional payloads to cells of behaving mammals. *Neuron* **107**, 836–853 (2020).
34. Deo, C. et al. The HaloTag as a general scaffold for far-red tunable chemigenetic indicators. *Nat. Chem. Biol.* **17**, 718–723 (2021).
35. Grimm, J. B. et al. A general method to fine-tune fluorophores for live-cell and in vivo imaging. *Nat. Methods* **14**, 987–994 (2017).
36. Jan, Y.-H. et al. Vitamin K3 (menadione) redox cycling inhibits cytochrome P450-mediated metabolism and inhibits parathion intoxication. *Toxicol. Appl. Pharmacol.* **288**, 114–120 (2015).
37. Loor, G. et al. Menadione triggers cell death through ROS-dependent mechanisms involving PARP activation without requiring apoptosis. *Free Radic. Biol. Med.* **49**, 1925–1936 (2010).
38. Criddle, D. N. et al. Menadione-induced reactive oxygen species generation via redox cycling promotes apoptosis of murine pancreatic acinar cells. *J. Biol. Chem.* **281**, 40485–40492 (2006).
39. Tongul, B. & Tarhan, L. The effect of menadione-induced oxidative stress on the in vivo reactive oxygen species and antioxidant response system of *Phanerochaete chrysosporium*. *Process Biochem.* **49**, 195–202 (2014).
40. Lim, J. B., Langford, T. F., Huang, B. K., Deen, W. M. & Sikes, H. D. A reaction–diffusion model of cytosolic hydrogen peroxide. *Free Radic. Biol. Med.* **90**, 85–90 (2016).
41. Heppert, J. K. et al. Comparative assessment of fluorescent proteins for in vivo imaging in an animal model system. *Mol. Biol. Cell* **27**, 3385–3394 (2016).
42. Campbell, B. C. et al. mGreenLantern: a bright monomeric fluorescent protein with rapid expression and cell filling properties for neuronal imaging. *Proc. Natl Acad. Sci. USA* **117**, 30710–30721 (2020).
43. Schweikhard, V. et al. Application note: the Power HyD family of detectors. *Nat. Methods* https://www.nature.com/articles/d42473-020-00398-0 (2020).
44. Lambert, T. J. FPbase: a community-editable fluorescent protein database. *Nat. Methods* **16**, 277–278 (2019).
45. Yamada, Y. & Mikoshiba, K. Quantitative comparison of novel GCaMP-type genetically encoded Ca^{2+} indicators in mammalian neurons. *Front. Cell Neurosci.* **6**, 41 (2012).
46. Han, L. et al. RFP tags for labeling secretory pathway proteins. *Biochem. Biophys. Res. Commun.* **447**, 508–512 (2014).
47. Abdelfattah, A. S. et al. A bright and fast red fluorescent protein voltage indicator that reports neuronal activity in organotypic brain slices. *J. Neurosci.* **36**, 2458–2472 (2016).
48. Costantini, L. M., Fossati, M., Francolini, M. & Snapp, E. L. Assessing the tendency of fluorescent proteins to oligomerize under physiologic conditions: fluorescent protein oligomerization assay. *Traffic* **13**, 643–649 (2012).
49. Belousov, V. V. et al. Genetically encoded fluorescent indicator for intracellular hydrogen peroxide. *Nat. Methods* **3**, 281–286 (2006).
50. Taniguchi, J. et al. Comment on 'Accumbens cholinergic interneurons dynamically promote dopamine release and enable motivation'. *eLife* **13**, e95694 (2024).
51. Heim, R., Prasher, D. C. & Tsien, R. Y. Wavelength mutations and posttranslational autoxidation of green fluorescent protein. *Proc. Natl Acad. Sci. USA* **91**, 12501–12504 (1994).
52. Ma, Y., Sun, Q. & Smith, S. C. The mechanism of oxidation in chromophore maturation of wild-type green fluorescent protein: a theoretical study. *Phys. Chem. Chem. Phys.* **19**, 12942–12952 (2017).
53. Takahashi, E. et al. Genetic oxygen sensor: GFP as an indicator of intracellular oxygenation. *Adv. Exp. Med. Biol.* **566**, 39–44 (2005).
54. Ishii, T., Warabi, E. & Mann, G. E. Mechanisms underlying NRF2 nuclear translocation by non-lethal levels of hydrogen peroxide: p38 MAPK-dependent neutral sphingomyelinase2 membrane trafficking and ceramide/PKCζ/CK2 signaling. *Free Radic. Biol. Med.* **191**, 191–202 (2022).
55. Covas, G., Marinho, H. S., Cyrne, L. & Antunes, F. Activation of NRF2 by H_2O_2: de novo synthesis versus nuclear translocation. *Methods Enzymol.* **528**, 157–171 (2013).
56. Görlach, A., Bertram, K., Hudecova, S. & Krizanova, O. Calcium and ROS: a mutual interplay. *Redox Biol.* **6**, 260–271 (2015).
57. Nikolaienko, R., Bovo, E. & Zima, A. V. Redox dependent modifications of ryanodine receptor: basic mechanisms and implications in heart diseases. *Front. Physiol.* **9**, 1775 (2018).
58. Johnstone, V. P. A. & Hool, L. C. Glutathionylation of the L-type Ca^{2+} channel in oxidative stress-induced pathology of the heart. *Int. J. Mol. Sci.* **15**, 19203–19225 (2014).
59. Gonnot, F. et al. SERCA2 phosphorylation at serine 663 is a key regulator of Ca^{2+} homeostasis in heart diseases. *Nat. Commun.* **14**, 3346 (2023).
60. Goodman, J. B. et al. Redox-resistant SERCA [sarco(endo)plasmic reticulum calcium ATPase] attenuates oxidant-stimulated mitochondrial calcium and apoptosis in cardiac myocytes and pressure overload-induced myocardial failure in mice. *Circulation* **142**, 2459–2469 (2020).

61. Akaike, T. et al. A sarcoplasmic reticulum localized protein phosphatase regulates phospholamban phosphorylation and promotes ischemia reperfusion injury in the heart. *JACC Basic Transl. Sci.* **2**, 160–180 (2017).
62. Varghese, E. & Büsselberg, D. Auranofin, an anti-rheumatic gold compound, modulates apoptosis by elevating the intracellular calcium concentration ($[Ca^{2+}]_i$) in MCF-7 breast cancer cells. *Cancers* **6**, 2243–2258 (2014).
63. Harper, M. T. Auranofin, a thioredoxin reductase inhibitor, causes platelet death through calcium overload. *Platelets* **30**, 98–104 (2019).
64. Kernik, D. C. et al. A computational model of induced pluripotent stem-cell derived cardiomyocytes incorporating experimental variability from multiple data sources. *J. Physiol.* **597**, 4533–4564 (2019).
65. Lee, Y.-K. et al. Calcium homeostasis in human induced pluripotent stem cell-derived cardiomyocytes. *Stem Cell Rev. Rep.* **7**, 976–986 (2011).
66. Tu, C., Chao, B. S. & Wu, J. C. Strategies for improving the maturity of human induced pluripotent stem cell-derived cardiomyocytes. *Circ. Res.* **123**, 512–514 (2018).
67. Goversen, B., van der Heyden, M. A. G., van Veen, T. A. B. & de Boer, T. P. The immature electrophysiological phenotype of iPSC-CMs still hampers in vitro drug screening: special focus on I_{K1}. *Pharmacol. Ther.* **183**, 127–136 (2018).
68. Itzhaki, I. et al. Calcium handling in human induced pluripotent stem cell derived cardiomyocytes. *PLoS ONE* **6**, e18037 (2011).
69. Koivumäki, J. T. et al. Structural immaturity of human iPSC-derived cardiomyocytes: in silico investigation of effects on function and disease modeling. *Front. Physiol.* **9**, 80 (2018).
70. Kritsiligkou, P. et al. Proteome-wide tagging with an H_2O_2 biosensor reveals highly localized and dynamic redox microenvironments. *Proc. Natl Acad. Sci. USA* **120**, e2314043120 (2023).
71. Montiel, V. et al. Inhibition of aquaporin-1 prevents myocardial remodeling by blocking the transmembrane transport of hydrogen peroxide. *Sci. Transl. Med.* **12**, eaay2176 (2020).
72. Schattauer, S. S. et al. Peroxiredoxin 6 mediates $G\alpha_i$ protein-coupled receptor inactivation by cJun kinase. *Nat. Commun.* **8**, 743 (2017).
73. Schattauer, S. S. et al. Reactive oxygen species (ROS) generation is stimulated by κ opioid receptor activation through phosphorylated c-Jun N-terminal kinase and inhibited by p38 mitogen-activated protein kinase (MAPK) activation. *J. Biol. Chem.* **294**, 16884–16896 (2019).
74. Terzi, A. & Suter, D. M. The role of NADPH oxidases in neuronal development. *Free Radic. Biol. Med.* **154**, 33–47 (2020).
75. Ma, M. W. et al. NADPH oxidase in brain injury and neurodegenerative disorders. *Mol. Neurodegener.* **12**, 7 (2017).
76. Schröder, K. NADPH oxidases: current aspects and tools. *Redox Biol.* **34**, 101512 (2020).
77. Sies, H. et al. Defining roles of specific reactive oxygen species (ROS) in cell biology and physiology. *Nat. Rev. Mol. Cell Biol.* **23**, 499–515 (2022).
78. Miller, E. W., Dickinson, B. C. & Chang, C. J. Aquaporin-3 mediates hydrogen peroxide uptake to regulate downstream intracellular signaling. *Proc. Natl Acad. Sci. USA* **107**, 15681–15686 (2010).
79. Thiagarajah, J. R., Chang, J., Goettel, J. A., Verkman, A. S. & Lencer, W. I. Aquaporin-3 mediates hydrogen peroxide-dependent responses to environmental stress in colonic epithelia. *Proc. Natl Acad. Sci. USA* **114**, 568–573 (2017).
80. Haskew-Layton, R. E. et al. Controlled enzymatic production of astrocytic hydrogen peroxide protects neurons from oxidative stress via an NRF2-independent pathway. *Proc. Natl Acad. Sci. USA* **107**, 17385–17390 (2010).
81. Niemczyk, E. et al. A possible involvement of plasma membrane NAD(P)H oxidase in the switch mechanism of the cell death mode from apoptosis to necrosis in menadione-induced cell injury. *Acta Biochim. Pol.* **51**, 1015–1022 (2004).
82. Thor, H. et al. The metabolism of menadione (2-methyl-1,4-naphthoquinone) by isolated hepatocytes. A study of the implications of oxidative stress in intact cells. *J. Biol. Chem.* **257**, 12419–12425 (1982).
83. Yamashoji, S., Ikeda, T. & Yamashoji, K. Extracellular generation of active oxygen species catalyzed by exogenous menadione in yeast cell suspension. *Biochim. Biophys. Acta* **1059**, 99–105 (1991).
84. Suzuki, Y. & Ono, Y. Involvement of reactive oxygen species produced via NADPH oxidase in tyrosine phosphorylation in human B- and T-lineage lymphoid cells. *Biochem. Biophys. Res. Commun.* **255**, 262–267 (1999).
85. Shu, X. et al. A genetically encoded tag for correlated light and electron microscopy of intact cells, tissues, and organisms. *PLoS Biol.* **9**, e1001041 (2011).
86. Barnett, M. E., Baran, T. M., Foster, T. H. & Wojtovich, A. P. Quantification of light-induced miniSOG superoxide production using the selective marker, 2-hydroxyethidium. *Free Radic. Biol. Med.* **116**, 134–140 (2018).
87. Seo, M. J. et al. Dual inhibition of thioredoxin reductase and proteasome is required for auranofin-induced paraptosis in breast cancer cells. *Cell Death Dis.* **14**, 42 (2023).
88. Renken, S. et al. Targeting of NRF2 improves antitumoral responses by human NK cells, TIL and CAR T cells during oxidative stress. *J. Immunother. Cancer* **10**, e004458 (2022).
89. Koren, S. A. et al. All-optical spatiotemporal mapping of ROS dynamics across mitochondrial microdomains in situ. *Nat. Commun.* **14**, 6036 (2023).
90. Woo, H. A. et al. Inactivation of peroxiredoxin I by phosphorylation allows localized H_2O_2 accumulation for cell signaling. *Cell* **140**, 517–528 (2010).
91. DeYulia, G. J. Jr, Cárcamo, J. M., Bórquez-Ojeda, O., Shelton, C. C. & Golde, D. W. Hydrogen peroxide generated extracellularly by receptor–ligand interaction facilitates cell signaling. *Proc. Natl Acad. Sci. USA* **102**, 5044–5049 (2005).
92. Xu, C., Peng, B. & Liu, S. Using intra-brain drug infusion to investigate neural mechanisms underlying reward-seeking behavior in mice. *STAR Protoc.* **3**, 101221 (2022).
93. Xavier, A. L. R. et al. Cannula implantation into the cisterna magna ofrodents. *J. Vis. Exp.* https://doi.org/10.3791/57378 (2018).
94. Farrants, H. et al. A modular chemigenetic calcium indicator for multiplexed in vivo functional imaging. *Nat. Methods* **21**, 1916–1925 (2024).
95. Grimm, J. B. et al. A general method to optimize and functionalize red-shifted rhodamine dyes. *Nat. Methods* **17**, 815–821 (2020).

[1]Molecular Engineering and Sciences Institute, University of Washington, Seattle, WA, USA. [2]Department of Bioengineering, University of Washington, Seattle, WA, USA. [3]Institute for Stem Cell and Regenerative Medicine, University of Washington, Seattle, WA, USA. [4]Department of Chemical Engineering, University of Washington, Seattle, WA, USA. [5]Department of Biochemistry, University of Washington, Seattle, WA, USA. [6]Institute for Protein Design, University of Washington, Seattle, WA, USA. [7]Center for Translational Muscle Research, University of Washington, Seattle, WA, USA. [8]Center for Cardiovascular Biology, University of Washington, Seattle, WA, USA. [9]Department of Laboratory Medicine and Pathology, University of Washington, Seattle, WA, USA. [10]Division of Cardiology, University of Washington, Seattle, WA, USA. [11]Howard Hughes Medical Institute, University of Washington, Seattle, WA, USA. [12]Department of Rehabilitation Medicine, University of Washington, Seattle, WA, USA. [13]These authors contributed equally: Chelsea E. Gibbs, Zheyu Ruby Jin, Yuxuan Wang. ✉e-mail: berndtuw@uw.edu

Methods

Ethics statement

This study was performed in strict accordance with the recommendations in the Guide for the Care and Use of Laboratory Animals of the National Institutes of Health. All animals were handled according to the approved Institutional Animal Care and Use Committee protocols 4422-01 and 4383-02 of the University of Washington and followed the National Institute of Health and the Association for Assessment and Accreditation of Laboratory Animal Care International guidelines. The University of Washington has an approved Animal Welfare Assurance (A3464) on file with the National Institute of Health Office of Laboratory Animal Welfare, is registered with the US Department of Agriculture (certificate 91-R-0001) and is accredited by the American Association for Accreditation of Laboratory Animal Care International.

Statistics and reproducibility

Most experiments were conducted with at least three independent biological replicates ($n \geq 3$), ensuring robustness and reproducibility. Raw data and descriptive statistics for all presented analyses are also available on figshare (https://doi.org/10.6084/m9.figshare.28306691)[96], and automated quantification methods were used where possible to minimize user bias. Data processing and statistical analyses were performed using Python (NumPy, SciPy and Seaborn), with Seaborn v0.13.2 used for statistical visualization. Error bars and bands in the plots represent the 95% bootstrap ($n = 1{,}000$) CI of the mean, estimated through resampling, whereas box plots display the median, IQR, whiskers (extending to 1.5× IQR) and outliers. A two-sided independent *t*-test was used for statistical comparisons. The complete minimal raw dataset and code for downstream analyses and visuals generated for this study are publicly available on figshare (https://doi.org/10.6084/m9.figshare.28306691)[96] to facilitate reproducibility. Data distribution was assumed to be normal but was not formally tested. Although data collection and analysis were not performed blind to experimental conditions, we used a high-throughput computational pipeline for unbiased extraction of fluorescence data using FUSE v0.1.0-alpha[97].

Molecular biology

oROS-HT variants were all cloned based on the pC1 plasmid backbone from pC1-HyPer-Red (Addgene ID 48249) and insertion from pAAV-synapsin-HaloCaMP1a-EGFP (Addgene ID 138327). Primers for point mutations or fragment assembly required to generate the oROS-HT screening variants were designed for the In Vitro Assembly cloning technique[98], and they were ordered from Integrated DNA Technologies. All gene fragment amplification was performed using SuperFi-II polymerase (Invitrogen, 12368010). Amplification of DNA fragments was verified by agarose gel electrophoresis. Thirty minutes of DpnI enzyme treatment was performed on every PCR product to remove the plasmid template from PCR samples. Circularization or assembly of the PCR products was achieved with the In Vitro Assembly cloning technique, and linear DNA products were transformed into competent *E. coli* cells (DH5α or TOP10) and grown on agar plates that contained kanamycin selection antibiotic (50 μg ml^{-1}). Following colony formation, single colonies were picked and grown in 5-ml cultures containing LB broth (Fisher BioReagents, BP9723-2) and selection antibiotic (kanamycin; 50 μg ml^{-1}) overnight (37 °C, 230 rpm). DNA was isolated using Machery Nagel DNA prep kits (Machery Nagel, 740490.250). Sanger sequencing (Genewiz) or whole-plasmid Nanopore sequencing (Plasmidsaurus) of isolated plasmid DNA was used to confirm the presence of the intended mutation. Genes encoding the final variants were cloned into a CAG-driven backbone, pCAG-Archon1-KGC-EGFP-ER2-WPRE (Addgene, 108423), using the methods described above. All subsequences were verified by Sanger sequencing (Genewiz) or whole-plasmid Nanopore sequencing (Plasmidsarus). Additionally, pC1-CMV-mito-DAAO (Addgene ID 141132) and pC1-SypHer3s-IMS (Addgene ID 108120) were generously provided by Addgene. The miniSOG1 gene fragment was ordered from Twist Bioscience based on miniSOG-C1 (Addgene ID 54821) and replaced oROS-HT in pC1-dmito-oROS-HT and pDisplay-oROS-HT.

Protein structure prediction and analysis

Protein structure analysis and plotting were performed using Chimera-X-1.7.1. Oxidized (PDB ID 1I6A) and reduced (PDB ID 1I69) crystal structures of ecOxyR were imported from the PDB. Pairwise residue distance between reduced and oxidized ecOxyR structures was determined by aligning both structures using a matchmaker algorithm that superimposes protein structures by creating a pairwise sequence alignment and then fitting the aligned residue pairs to derive pairwise residue distances. The structure of variant 213–214 was predicted using ColabFold[29] (msa_method = mmseqs2, homooligomer = 1 or 2, pair_msa = false, max_msa = 512:1,024, subsample_msa = true, num_relax = none or 1, use_turbo = true, use_ptm = true, rank_by = pLDDT, num_models = 3 or 5, num_samples = 1, num_ensemble = 1, max_recycles = 6, 24, 48, tol = 0, is_training = false, use_templates = false). The putative position of JF635 was incorporated into the ColabFold prediction of variant 213–214 to report the JF635-bound cpHaloTag structure (PDB ID 6U2M) with the matchmaker algorithm.

Chemicals

HaloTag ligands of JF (JF-HTLs) 635 and 585 described in this paper were generously provided by Janelia Materials. Stock solutions of JF-HTLs were prepared in 100% DMSO at 200 μM. Cells described in this study were incubated in 200 nM JF-HTL for 1 h before imaging unless specified. Although washout of the dyes is not required, we switched the cells into imaging medium before imaging. H_2O_2 working solutions were freshly prepared before every experiment from 30% (wt/wt) H_2O_2 solution in water (Sigma-Aldrich, H1009). A stock solution of menadione (Sigma-Aldrich, M9429) was prepared in 100% DMSO at 50 mM. A stock solution of auranofin (Tocris Bioscience, 46-005-0) was prepared in 100% DMSO at 50 mM.

Protein purification

oROS-HT was expressed in the New England Biolabs BL21(DE3) *E. coli* strain using the pET29b vector. An overnight LB culture, started from a single colony, was diluted 1:100 in TBII (MpBio) medium supplemented with 50 μg ml^{-1} kanamycin. A total of 1,500 ml of expression culture was grown at 37 °C for 4 h, followed by induction with isopropyl-β-D-thiogalactopyranoside and continued culturing at 18 °C for 24 h with shaking at 225 rpm. Cells were then collected by centrifugation at 4,000*g* and resuspended in 50 mM Tris (pH 8.0), 300 mM NaCl, 20 mM imidazole, 1 mM PMSF, 100 μg ml^{-1} lysozyme (Sigma-Aldrich) and 10 μg ml^{-1} DNase (Sigma-Aldrich). Cells were lysed by sonication and centrifuged at approximately 18,000*g* for 30 min. The soluble fractions were purified using immobilized metal affinity chromatography with gravity columns packed with Ni-NTA agarose resin (Qiagen). Columns were washed with a buffer containing 20 mM imidazole, and proteins were eluted with a buffer containing 300 mM imidazole and 1.5 mM DTT. Proteins were further purified by size-exclusion chromatography using an ÄKTA FPLC instrument equipped with a Superdex 200 Increase 10/300 GL column (GE Healthcare Life Sciences) equilibrated with 25 mM Tris (pH 8.0), 150 mM NaCl and 1.5 mM DTT.

Fluorimetry of oROS-HT$_{635}$ following attachment with JF635-HTL

Experiments to determine the quantum yield of oROS-HT$_{635}$ were conducted using a FluoroMax-4 spectrofluorometer (Horiba). Before measurements, oROS-HT$_{635}$ (1.5 μM) was incubated with JF635-HTL (2 μM) in a solution containing 25 mM Tris (pH 8.0), 150 mM NaCl and 1.5 mM DTT at room temperature for 1 h. To determine the quantum yield of fluorescence of oROS-HT$_{635}$, the emission spectra of the fluorescence excited at 635 nm were measured and compared to Nile blue dye as a standard.

Cellular brightness comparison

Experiments comparing the cellular brightness of oROS-HT$_{635}$ and HyPerRed were conducted using HEK293 cells expressing eGFP tandem fusions (C termini) of each sensor. Imaging was performed on a Stellaris Falcon Confocal system (Leica Microsystems) with an HC PL APO CS2 ×20/0.75-NA dry objective. Consistent imaging parameters were used across all measurements, including unidirectional scan speed (400 Hz), pixel dwell time (1.41 µs) and photon counting mode via the HyD X detector. To minimize autofluorescence artifacts, pixels were Tau gated for fluorescence lifetimes of 1.04–8 ns. Image segmentation was performed using Cellpose, enabling downstream analysis of average photon counts per cell. For 10-nm spectral peak bandpass-based brightness comparisons between HyPerRed (excitation of 575 nm and emission of 600–610 nm) and oROS-HT$_{635}$ (excitation of 640 nm and emission of 650–660 nm), photon counts were normalized to their respective tandem eGFP (excitation of 488 nm and emission of 508–518 nm) fluorescence. All three fluorophores were excited with ~49-µW laser power from a white-light laser (Leica; set to 85% maximum power). Extracted average photon counts per cell were further corrected for spectral effects (that is, shorter wavelengths correspond to higher energy photons) and the published photon detection efficiency of the HyD X detector[97]. Lambda scans of oROS-HT$_{635}$ (excitation of 640 nm and emission of 650–800 nm, 10-nm bandpass) and HyPerRed (excitation of 575 nm and emission of 585–735 nm; 10-nm bandpass) were performed using identical arbitrary laser power settings. These scans were normalized to the actual excitation photon flux measured with an optical power meter. Finally, photon counts from the lambda scans were normalized to those of each sensor's tandem eGFP.

Organized smooth endoplasmic reticulum assay

CytERM-mTurquoise2 (Addgene ID 98833) and CytERM-dTomato (Addgene ID 98834) were used as negative and positive controls, respectively, to perform the OSER assay and compare monomericity of oROS-HT$_{635}$ and HyPerRed. Both sensors were cloned into the CytERM plasmid for expression in HEK293 cells via lipofection. Images for OSER assessment were acquired using a Leica SP8 confocal microscope from the Imaging Core in the Institute of Stem Cell and Regenerative Medicine. Cells with or without whorl structures were manually counted to derive the OSER ratio.

Mammalian cells

HEK293 cells (ATCC, CRL-1573) were cultured in DMEM supplemented with GlutaMAX (Gibco, 10569-010) and 10% fetal bovine serum (Biowest, S1620). When cultures reached 85% confluency, the cultures were seeded at 150,000 or 75,000 cells per well in 24- or 48-well plates, respectively. Twenty-four hours after cell seeding, the cells were transfected using Lipofectamine 3000 (Invitrogen, L3000015) at 1,000 or 500 ng of DNA per well of a 24- or 48-well plate, according to the manufacturer's instructions. For dual-transfection experiments, 1:1 (equiv. mass) plasmid cocktails were made for the transfection. Primary cortical neurons were prepared as previously described[99,100] and maintained in Neuronal Basal Medium (Invitrogen, 10888022) supplemented with B-27 (Invitrogen, 17504044) and glutamine (Invitrogen, 35050061) every 3 days and transduced with crude AAV9-CAG-oROS-HT produced by the Fred Hutchinson Cancer Research Center Vector Production Core.

Brain slice imaging

Organotypic whole-hemisphere rat brain slice preparation. Male rats on postnatal day 10 were administered an overdose intraperitoneal injection of pentobarbital (120–150 mg per kg (body weight)). Animals were then quickly decapitated, and whole brains were extracted, cut into hemispheres and placed into ice-cold dissecting medium consisting of 0.64% (wt/vol) glucose, 100% HBSS and 1% penicillin–streptomycin. Whole-hemisphere live slices (300 µm) were obtained using a tissue chopper, as previously described[101]. Slices were then transferred to 35-mm, 0.4-µm-pore membrane inserts in six-well plates and cultured in 1 ml of 5% heat-inactivated horse-serum slice culture medium consisting of 50% MEM, 45% HBSS, 1% GlutaMAX and 1% penicillin–streptomycin. Slices were cultured in a sterile incubator at a constant temperature (37 °C), humidity and CO_2 level (5%).

Adeno-associated virus transduction and confocal imaging. After 1 day in vitro, a crude AAV9-CAG-oROS-HT preparation was added to the brain slices. At the end of the 3-day incubation, 1 µM JF635-HTL was added to the slices for an additional 48 h. Organotypic whole-hemisphere brain slices were transferred to 35-mm confocal dishes (VWR, 75856-742). Confocal images were acquired at ×10 (Nikon Plan Apo ×10/0.45-NA objective) and ×20 (Nikon Plan Apo ×20/0.75-NA objective) magnifications (Nikon Corporation). Brain slice tile scans were obtained with the Cy5 channel before multiple representative images were acquired from both the cortex and striatum of each slice. Image acquisition settings were kept consistent before and after stimulation with 300 µM H_2O_2.

Differentiation of stem cell-derived cardiomyocytes and neurons

Human induced pluripotent stem cell culture and cardiomyocyte differentiation (diffusion study). Undifferentiated IMR90 (WiCell) hiPS cells were maintained on Matrigel-coated (Corning) tissue culture plates in mTeSR1 (Stemcell Technologies). Cardiomyocyte-directed differentiation was performed using a modified small-molecule Wnt-modulating protocol using Chiron 99021 and IWP-4 as previously described[102,103]. Lactate enrichment was performed following differentiation to purify hiPS cell-CMs[104].

Human induced pluripotent stem cell culture and cardiomyocyte differentiation (auranofin study). Undifferentiated hiPS cells (WTC11, male) were maintained on Matrigel-coated (Corning) tissue culture plates in mTeSR1 (Stemcell Technologies). Cardiomyocyte-directed differentiation was performed using the Roswell Park Memorial Institute (RPMI) medium, bovine serum albumin and ascorbic acid)-based modified method as previously described[105]. Spontaneous contraction was observed on day 8 after induction. On day 12 after induction, the medium was reduced to 1 ml in preparation for 45 min of heat shock at 42 °C on day 13. After heat shock, the medium was changed to 1 ml of fresh RPMI + B-27 + insulin. On day 14, cells were dissociated with 0.05% Trypsin (Thermo Fisher) and frozen in BAMBANKER for storage in liquid nitrogen. The cardiomyocytes were thawed in 90% RPMI + B-27 + insulin and 10% Knockout Serum with 10 µM ROCK inhibitor and plated on Matrigel-coated plates. Twenty-four hours after thawing, the medium was replaced with fresh RPMI + B-27 + insulin and changed every other day.

Human induced pluripotent stem cell culture and cortical neuron differentiation. Cortical cultures were generated from the previously characterized wild-type J. Craig Venter background hiPS cell line[106–108]. Neural progenitor cells (NPCs) from this cell line were differentiated from hiPS cells using dual-SMAD inhibition, and NPCs were differentiated into neurons as previously described[107,108]. Briefly, for cortical culture differentiation from NPCs, NPCs were expanded into 10-cm plates in basal neural maintenance medium (1:1 DMEM/F12; Life Technologies, 11039047) + glutamine medium/neurobasal medium (Gibco, 21103049), 0.5% N2 supplement (Thermo Fisher Scientific, 17502-048), 1% B-27 supplement (Thermo Fisher Scientific, 17504-044), 0.5% GlutaMAX (Thermo Fischer Scientific, 35050061), 0.5% insulin–transferrin–selenium (Thermo Fisher Scientific, 41400045), 0.5% nonessential amino acids (Thermo Fisher Scientific, 11140050), 0.2% β-mercaptoethanol (Life Technologies, 21985023) and 20 ng m^{-1} fibroblast growth factor (R&D Systems). Once the NPCs reached 100% confluence, they were switched to neural differentiation medium (basal neural maintenance medium + 0.2 mg ml^{-1} brain-derived neurotrophic factor (PeproTech, 450-02) + 0.2 mg ml^{-1} glial cell-derived neurotrophic factor (PeproTech, 450-10) + 0.5 M dbcAMP (Sigma-Aldrich, D0260)). Neural differentiation medium was changed twice a week for 21 days, at which point the differentiation was considered finished. To isolate neurons from cortical cultures, we performed bead sorting purification (BD BioSciences, 557899) selecting against CD44$^+$, CD184$^+$ and CD271$^+$ cells (550989, 557145 and 557196, respectively, BD BioSciences). Purified neurons were plated in a 96-well plate at a density of 200,000 cells per well.

Immunofluorescence staining

Immunofluorescence staining of NRF2 was performed using polyclonal anti-NRF2 (PA5-27882, Invitrogen) and donkey anti-rabbit IgG Alexa Fluor 488 (A21206, Invitrogen). HEK293 cells for each condition were fixed in 4% paraformaldehyde for 15 min and permeabilized in 0.2% Triton X-100 solution for 1 h. After blocking the fixed cells for 1 h with 0.5% bovine serum albumin blocking buffer in Tris-buffered saline with Tween 20, cells were then incubated with primary antibody diluted (1:200) in blocking buffer overnight at 4 °C. The next day, cells were washed three times with PBS and incubated in a solution containing secondary antibodies diluted (1:1,000) in 0.5% bovine serum albumin in PBS overnight at 4 °C. Counterstaining was performed with VECTASHIELD containing DAPI (Vector Labs).

Microscopy

Imaging experiments described in this study were performed as follows unless specifically noted. Epifluorescence imaging experiments were performed on a Leica DMI8 microscope (Semrock bandpass filter: GFP ratio excitation/emission: FF01-391-23/FF01-520-35, GFP excitation/emission: FF01-474-27/FF01-520-35, RFP excitation/emission: FF01-554-23 or FF01-578-21/FF01-600-37, far-red excitation/emission: FF01-635-18/FF01-680-42) controlled by MetaMorph Imaging software, using a sCMOS camera (Photometrics Prime95B) and a ×20 magnification lens (Leica HCX PL FLUOTAR L ×20/0.40-NA CORR) or ×10 objective (Leica HC PL FLUOTAR L ×10/0.32-NA). Confocal imaging experiments were performed on a Leica SP8 confocal microscope located in the Imaging Core at the Institute of Stem Cell and Regenerative Medicine. Cells were imaged in live-cell imaging solution with 10 mM glucose (LCIS+, Gibco, A14291DJ).

Hypoxic oROS-HT$_{635}$ sensor maturation in HEK293 cells

Two days after seeding of HEK293 cells in 24-well plates (150,000 cells per well), culture medium was swapped from complete DMEM medium (as mentioned above) to complete Fluorobrite DMEM (A1896701, Gibco) with 20 mM HEPES. After 2 h of acclimation, cells were transfected (Lipofectamine based, as described above) with pC1-oROS-HT-C199S (loss of function) with 100 nM JF635-HTL. Immediately after transfection, transfected cells were either incubated at 37 °C in an atmospheric environment or under hypoxic conditions. For hypoxic conditions, culture plates were transferred into a sealable chamber. The chamber was flushed with N_2 for 10 min at a flow rate of 10 l min^{-1} before being placed into the incubator. Approximately 18 h later, epifluorescence imaging was performed as described earlier.

Multiplexed experiments

oROS-HT$_{635}$/SypHer3s. HEK293 cells with pC1-oROS-HT/pC1-SypHer3s or pC1-oROS-HT-C199S/pC1-SypHer3s co-transfection were imaged using an epifluorescence microscope. Described pH experiments were performed in PBS (10010001, Gibco) prepared at the reported pH. Fluorescence levels for GFP and far-red profiles were captured at 0.67 Hz or 0.5 Hz.

oROS-HT$_{635}$/GRX1–roGFP2. HEK293 cells co-transfected with pC1-oROS-HT and pC1-GRX1-roGFP2 in live-cell imaging solution with 10 mM glucose (LCIS+, Gibco, A14291DJ) were imaged using an epifluorescence microscope. For the sequential response of oROS-HT/GRX1–roGFP2 to 10 μM H_2O_2, fluorescence levels for GFP and far-red profiles were captured every second. To assess responses to auranofin, fluorescence levels for GFP ratio, GFP and far-red profiles were captured every minute.

oROS-HT$_{635}$/Fluo-4. hiPS cell-CMs were incubated with Fluo-4 (Invitrogen, F14201) at 5 μM and JF635-HTL in RPMI + B-27 + insulin for 1 h before imaging. To assess responses to auranofin, fluorescence levels of GFP (10 Hz) and far-red (0.1 Hz) profiles were acquired every 10 s for hiPS cell-CMs in HEPES-buffered RPMI + B-27 + insulin.

oROS-HT$_{635}$/oROS-G. Menadione-induced responses of pDisplay-oROS-HT and cytosolic oROS-G-expressing HEK293 cells (co-transfection) were imaged at 1 Hz. Fluorescence responses from responsive cells were extracted for downstream analysis. Visualization of paracrine H_2O_2 using oROS-HT- and oROS-G-expressing HEK293 cells (coculture of cells expressing each sensor) was imaged at 0.25 Hz.

oROS-HT$_{635}$/miniSOG. To induce light-sensitive generation of superoxide using miniSOG, HEK293 cells expressing both miniSOG (dMito or pDisplay tagged) and CAAX-oROS-HT were exposed to two separate 5-s-long illuminations (~8.15 mW mm^{-2}) with GFP excitation profiles described above.

Analysis

Analysis of cell fluorescence imaging data was performed using FUSE, a custom cloud-based semiautomated time series fluorescence data analysis platform written in Python. First, the cell segmentation quality of the selected Cellpose[109] model was manually verified. For the segmentation of cells expressing cytosolic fluorescent indicators, model 'cyto' was selected as our base model. If the selected Cellpose model was low performing, we further trained the Cellpose model using the Cellpose 2.0 human-in-the-loop system[110]. Using an optimized segmentation model, fluorescence time series data were extracted for each region of interest. This allows for unbiased extraction of change in cellular fluorescence information for a complete set of experimental samples. Extracted fluorescence data were normalized as specified in the text using a custom Python script. For subcellular-targeted oROS-HT$_{635}$, pixels positive for sensor expression were extracted to minimize bias from background pixels, which may arise due to varying morphology. The specific method and code for the NRF2 translocation assay are described in Supplementary Fig. 8 and on figshare (https://doi.org/10.6084/m9.figshare.28306691)[96].

Computational cell-scale modeling

We used an existing model of iPS cell-CM membrane kinetics[64] with one modification. Based on experimental observations, the spontaneous beating of the iPS cell-CMs was observed to be around 0.5 Hz. To reflect this observation in our computational simulations, we increased the maximal value of the inward rectifier potassium (I_{K1}) by a factor of 1.71484375 in the baseline version of the model. This change resulted in a decrease in spontaneous beating rate from 1.1 Hz to 0.5 Hz. The Kernik model comprises representations of major ionic currents, channels and pumps (intracellular ionic species tracked: Na^+, K^+ and Ca^{2+}). The SR is modeled as a distinct Ca^{2+}-rich intracellular compartment; trafficking of Ca^{2+} ions between the SR and the cytosol is mediated by three ionic fluxes: J_{up} (SR Ca^{2+} reuptake via the SR Ca^{2+} ATPase (SERCA2a)), J_{rel} (SR Ca^{2+} release via RyR2) and J_{leak} (passive Ca^{2+} leak from the SR into the cytosol). To simulate reactive oxygen species effects on iPS cell-CMs, we ran simulations in which we modified parameters corresponding to maximal efflux via SERCA2a, SR leak amplitude and maximal conductance of the I_{CaL}. The scaling factor for J_{up} (SERCA2a efflux) varied from 0.1 to 1.0 in steps of 0.1. Scaling factors for J_{leak} and I_{CaL} ranged from the default level (1.0) to 2.0 in steps of 0.1. Simulations of bioelectrical activity were conducted using openCARP[111], a cardiac electrophysiology modeling software that is freely available for non-commercial use (see http://opencarp.org/). All simulations were run for 100 s of simulated time, which we systematically confirmed was long enough for each perturbed version of the model to achieve a steady state (that is, zero beat-to-beat variability in membrane voltage or CaT shape). Simulated Ca_i time series values were postanalyzed with custom-written Python scripts. Scripts and files used to run all simulations can be found on figshare (https://doi.org/10.6084/m9.figshare.28306691)[96].

Reporting summary

Further information on research design is available in the Nature Portfolio Reporting Summary linked to this article.

Data availability

The complete minimal raw dataset from the experiments, representative images, downstream analysis and visualizations generated for this article are available on figshare at https://doi.org/10.6084/m9.figshare.28306691 (ref. 96). Plasmids for oROS-HT and its loss-of-function (C199S) and subcellular targeting variants described in this paper are available through Addgene at pC1-lifeact-oROS-HT (216420), pC1-IMS-oROS-HT (216419), pC1-dmito-oROS-HT (216418), pC1-oROS-HT-CaaX (216417), pDisplay-oROS-HT (216416), AAV2_CAG_oROS-HT(C199S)_WPRE (216415), AAV2_CAG_oROS-HT_WPRE (216414), pC1_oROS-HT (216413) and pC1_oROS-HT_LF(C199S) (216412). We will also provide plasmids upon request. The study accessed the PDB database (1I6A, 1I69 and 6U2M) for structural analysis. Source data are provided with this paper.

Code availability

Source code for simulation, data extraction, analysis and visualization is available on figshare at https://doi.org/10.6084/m9.figshare.28306691 (ref. 96).

References

96. Lee, J. D. et al. Data and code for "Monitoring in real time and far-red imaging of H_2O_2 dynamics with subcellular resolution". *figshare* https://doi.org/10.6084/m9.figshare.28306691 (2025).
97. Lee, J. D. et al. FUSE: fluorescent signal engine. *GitHub* https://github.com/justindaholee/FUSE (2025).
98. García-Nafría, J., Watson, J. F. & Greger, I. H. IVA cloning: a single-tube universal cloning system exploiting bacterial in vivo assembly. *Sci. Rep.* **6**, 27459 (2016).
99. Catapano, L. A., Arnold, M. W., Perez, F. A. & Macklis, J. D. Specific neurotrophic factors support the survival of cortical projection neurons at distinct stages of development. *J. Neurosci.* **21**, 8863–8872 (2001).
100. Martin, D. L. Synthesis and release of neuroactive substances by glial cells. *Glia* **5**, 81–94 (1992).
101. McKenna, M. et al. Organotypic whole hemisphere brain slice models to study the effects of donor age and oxygen-glucose-deprivation on the extracellular properties of cortical and striatal tissue. *J. Biol. Eng.* **16**, 14 (2022).
102. Lian, X. et al. Directed cardiomyocyte differentiation from human pluripotent stem cells by modulating Wnt/β-catenin signaling under fully defined conditions. *Nat. Protoc.* **8**, 162–175 (2013).
103. Bremner, S. B. et al. Full-length dystrophin deficiency leads to contractile and calcium transient defects in human engineered heart tissues. *J. Tissue Eng.* **13**, 20417314221119628 (2022).
104. Tohyama, S. et al. Distinct metabolic flow enables large-scale purification of mouse and human pluripotent stem cell-derived cardiomyocytes. *Cell Stem Cell* **12**, 127–137 (2013).
105. Yoo, D. *Studying the Role of Mechanical Contraction in Cardiac Muscle Development Using Genetically Engineered Non-Contractile Human Stem Cell-Derived Cardiomyocytes*. PhD thesis, Univ. of Washington (2021).
106. Young, J. E. et al. Elucidating molecular phenotypes caused by the SORL1 Alzheimer's disease genetic risk factor using human induced pluripotent stem cells. *Cell Stem Cell* **16**, 373–385 (2015).
107. Shin, Y. J. et al. Amyloid β peptides (Aβ) from Alzheimer's disease neuronal secretome induce endothelial activation in a human cerebral microvessel model. *Neurobiol. Dis.* **181**, 106125 (2023).
108. Knupp, A. et al. Depletion of the AD risk gene *SORL1* selectively impairs neuronal endosomal traffic independent of amyloidogenic APP processing. *Cell Rep.* **31**, 107719 (2020).
109. Stringer, C., Wang, T., Michaelos, M. & Pachitariu, M. Cellpose: a generalist algorithm for cellular segmentation. *Nat. Methods* **18**, 100–106 (2021).
110. Pachitariu, M. & Stringer, C. Cellpose 2.0: how to train your own model. *Nat. Methods* **19**, 1634–1641 (2022).
111. Plank, G. et al. The openCARP simulation environment for cardiac electrophysiology. *Comput. Methods Prog. Biomed.* **208**, 106223 (2021).

Acknowledgements

J.D.L. was supported by 1F31DA056121-01A1 and the ISCRM Fellowship. A.B. was supported by the Brain Research Foundation, UW Royalty Research Fund, UW ISCRM IPA, NIGMS R01 GM139850-01, P30 DA048736-01-Pilot, NIMH RF1MH130391, NINDS U01NS128537, NIDA R21DA051193 and the McKnight Foundation's Technologies in Neuroscience Award. S.J.W. was supported by the National Science Foundation DGE-2140004 and the Herbold Foundation. K.M.E. was supported by T32AG066574. A.A. was supported by the National Institute of General Medical Sciences grant RM1 GM131981, the National Institute of Arthritis and Musculoskeletal and Skin Diseases grant P30 AR074990, American Heart Association supplement grant AHA872208 and BCTP-NIH–NIBIB-5T32EB032787-02. We would like to thank the Janelia Materials program from Howard Hughes Medical Institute Janelia Research Campus for generous sharing of their Janelia Fluors essential for this study. This research received additional support from the Lynn and Mike Garvey Imaging Core, the UW NAPE Center, ISCRM Shared Equipment and Leica Center of Excellence for Cellular Imaging in Fred Hutch Cancer Research Center (H. West-Foyle and L. Schroeder). We also want to thank R. Moon for his support.

Author contributions

J.D.L. and A.B. conceived the study design and oROS-HT_{635} engineering strategies, performed experiments, and analyzed the data. J.D.L, A.N., S.Z. and A.S. cloned and screened the sensor variants. J.D.L., Y.W., A.M. and V.C. constructed constructs for chemigenetic/optogenetic demonstration of subcellular H_2O_2 and performed analysis. J.D.L, S.J.W. and H.C. performed purified protein assays and analysis. J.D.L., C.E.G. and P.M.B. performed in silico hiPS cell-CM simulations and analysis. J.D.L. and Z.R.J. performed maturation studies under hypoxia, and brain slice imaging and analysis. K.M.E., A.A., S.B.B., I.K.A.P. and C.A.W. differentiated and prepared hiPS cell-derived cells. A.B., P.M.B., E.N. D.L.M., J.E.Y., D.B., M.R. and F.M.-H. supervised the preparation of materials, experiments, analyses and paper writing.

Competing interests

The authors declare no competing interests.

Additional information

Supplementary information The online version contains supplementary material available at https://doi.org/10.1038/s41589-025-01891-7.

Correspondence and requests for materials should be addressed to Andre Berndt.

Peer review information *Nature Chemical Biology* thanks Marc Fransen, Celien Lismont and the other, anonymous, reviewer(s) for their contribution to the peer review of this work.

Reprints and permissions information is available at www.nature.com/reprints.

nature portfolio

Corresponding author(s): Andre Berndt
Last updated by author(s): 1/31/2025

Reporting Summary

Nature Portfolio wishes to improve the reproducibility of the work that we publish. This form provides structure for consistency and transparency in reporting. For further information on Nature Portfolio policies, see our Editorial Policies and the Editorial Policy Checklist.

Statistics

For all statistical analyses, confirm that the following items are present in the figure legend, table legend, main text, or Methods section.

n/a	Confirmed	
☐	☒	The exact sample size (*n*) for each experimental group/condition, given as a discrete number and unit of measurement
☐	☒	A statement on whether measurements were taken from distinct samples or whether the same sample was measured repeatedly
☐	☒	The statistical test(s) used AND whether they are one- or two-sided *Only common tests should be described solely by name; describe more complex techniques in the Methods section.*
☒	☐	A description of all covariates tested
☐	☒	A description of any assumptions or corrections, such as tests of normality and adjustment for multiple comparisons
☐	☒	A full description of the statistical parameters including central tendency (e.g. means) or other basic estimates (e.g. regression coefficient) AND variation (e.g. standard deviation) or associated estimates of uncertainty (e.g. confidence intervals)
☐	☒	For null hypothesis testing, the test statistic (e.g. *F*, *t*, *r*) with confidence intervals, effect sizes, degrees of freedom and *P* value noted *Give P values as exact values whenever suitable.*
☒	☐	For Bayesian analysis, information on the choice of priors and Markov chain Monte Carlo settings
☒	☐	For hierarchical and complex designs, identification of the appropriate level for tests and full reporting of outcomes
☒	☐	Estimates of effect sizes (e.g. Cohen's *d*, Pearson's *r*), indicating how they were calculated

Our web collection on statistics for biologists contains articles on many of the points above.

Software and code

Policy information about availability of computer code

Data collection	Metamorph v7.8.11.0, LAS X v4.7.0.28176, ChimeraX v1.7.1
Data analysis	The source codes are available via Figshare (DOI: 10.6084/m9.figshare.28306691)

For manuscripts utilizing custom algorithms or software that are central to the research but not yet described in published literature, software must be made available to editors and reviewers. We strongly encourage code deposition in a community repository (e.g. GitHub). See the Nature Portfolio guidelines for submitting code & software for further information.

Data

Policy information about availability of data

All manuscripts must include a data availability statement. This statement should provide the following information, where applicable:

- Accession codes, unique identifiers, or web links for publicly available datasets
- A description of any restrictions on data availability
- For clinical datasets or third party data, please ensure that the statement adheres to our policy

Complete minimal raw dataset from the experiments, downstream analysis, and visualizations generated for this article is available via Figshare (DOI: 10.6084/m9.figshare.28306691). Plasmids for oROS-HT and its loss-of-function (C199S) and subcellular targeting variants described in this paper are available through Addgene: pC1-lifeact-oROS-HT (#216420), pC1-IMS-oROS-HT (#216419), pC1-dmito-oROS-HT (#216418), pC1-oROS-HT-CaaX (#216417), pDisplay-oROS-HT

(#216416), AAV2_CAG_oROS-HT(C199S)_WPRE (#216415), AAV2_CAG_oROS-HT_WPRE (#216414), pC1_oROS-HT (#216413), pC1_oROS-HT_LF(C199S) (#216412). Authors will also provide plasmids upon request. The study accessed the PDB [:1I6A, 1I69, 6U2M] database for structural analysis.

Research involving human participants, their data, or biological material

Policy information about studies with human participants or human data. See also policy information about sex, gender (identity/presentation), and sexual orientation and race, ethnicity and racism.

Reporting on sex and gender	Biological sex of human cell lines used in the study is described in the method section.
Reporting on race, ethnicity, or other socially relevant groupings	N/A
Population characteristics	N/A
Recruitment	N/A
Ethics oversight	N/A

Note that full information on the approval of the study protocol must also be provided in the manuscript.

Field-specific reporting

Please select the one below that is the best fit for your research. If you are not sure, read the appropriate sections before making your selection.

☒ Life sciences ☐ Behavioural & social sciences ☐ Ecological, evolutionary & environmental sciences

For a reference copy of the document with all sections, see nature.com/documents/nr-reporting-summary-flat.pdf

Life sciences study design

All studies must disclose on these points even when the disclosure is negative.

Sample size	Sample sizes were determined empirically based on the nature of the fluorescence intensity data and the variability observed across independent trials. No formal statistical power calculation was performed prior to data collection; however, sample sizes were chosen to ensure robust statistical analysis and reproducibility. Specifically, samples (e.g., fluorescence intensity profiles of regions of interest or individual cells) were collected from fluorescence images obtained from independent trials, with data acquisition continuing until statistical significance was reached and typically beyond. Most datasets include hundreds of individual samples per condition, ensuring sufficient power to detect meaningful biological differences. To further enhance statistical robustness, we minimized technical bias through large sample sizes and an automated image analysis algorithm, FUSE, which provides unbiased quantification. The adequacy of sample sizes was confirmed post hoc through statistical analysis, ensuring that observed differences were not due to random variability.
Data exclusions	Cell segmentation and region of interest labeling was done both manually and computationally as described in the manuscript. Data point exhibiting abnormal intensity change induced by significant motion artifact (e.g. cell floating) were excluded from the analysis. For Figure 6c-d, fluorescence responses from responsive cells were extracted for downstream analysis.
Replication	Each in vitro data point contains samples from larger than 3 biological replicates unless noted. All attempts at replication were successful.
Randomization	The study primarily focused on analyzing a large number of samples and variants, with individual researchers overseeing all stages from experimental preparation to analysis. Sample allocation was not randomized because the study aimed to investigate predefined biological conditions rather than assess stochastic variability. Instead, experimental groups were assigned based on specific biological criteria, such as genetic variants or treatment conditions, ensuring systematic comparisons. To control for potential covariates, we maintained consistency in experimental conditions, including sample preparation, imaging parameters, and analysis pipelines. Additionally, we minimized technical bias through large sample sizes and an unbiased, automated image analysis algorithm, FUSE, which we describe in the Methods section. Given this approach, random allocation was not necessary, as the study did not rely on stochastic assignment but rather on predefined biological groupings.
Blinding	Data analysis was unbiased by an automated image analysis pipeline FUSE which automatically identified all sensor expressing cells using a deep-learning-based cell segmentation algorithm (CellPose) and extracted change in fluorescence from them.

Reporting for specific materials, systems and methods

We require information from authors about some types of materials, experimental systems and methods used in many studies. Here, indicate whether each material, system or method listed is relevant to your study. If you are not sure if a list item applies to your research, read the appropriate section before selecting a response.

Materials & experimental systems

n/a	Involved in the study
☐	☒ Antibodies
☐	☒ Eukaryotic cell lines
☒	☐ Palaeontology and archaeology
☐	☒ Animals and other organisms
☒	☐ Clinical data
☒	☐ Dual use research of concern
☒	☐ Plants

Methods

n/a	Involved in the study
☒	☐ ChIP-seq
☒	☐ Flow cytometry
☒	☐ MRI-based neuroimaging

Antibodies

Antibodies used	polyclonal Nrf2 antibody (PA5-27882, Invitrogen) and Donkey anti-Rabbit IgG Alexa Fluor 488 (A21206, Invitrogen).
Validation	PA5-27882 passed ThermoFisher's advanced verification. The Antibody was verified by Cell treatment to ensure that the antibody binds to the antigen stated. Published species: Human, Mouse, Pig, Rat, Zebrafish https://www.thermofisher.com/antibody/product/Nrf2-Antibody-Polyclonal/PA5-27882

Eukaryotic cell lines

Policy information about cell lines and Sex and Gender in Research

Cell line source(s)	HEK293 (ATCC: CRL-1573), IMR90 (WiCell, Female), WTC11(Male).
Authentication	HEK293 cell were authenticated by ATCC prior to shipping with STR profiling following ISO 9001 and ISO/IEC 17025 quality standards. We discard cells after 25 passages and start new cultures from P2 or P3 frozen stocks.
Mycoplasma contamination	HEK293, IMR90, WTC11 cells were tested negative for mycoplasma contamination.
Commonly misidentified lines (See ICLAC register)	Commonly misidentified lines were not used.

Animals and other research organisms

Policy information about studies involving animals; ARRIVE guidelines recommended for reporting animal research, and Sex and Gender in Research

Laboratory animals	Sprague-Dawley rats (virus antibody-free CD® (SD) IGS, Charles River Laboratories, Raleigh, NC, USA) postnatal day 10
Wild animals	No wild animals were used in the study.
Reporting on sex	Male and female mice were used. Detailed information available in the method section.
Field-collected samples	No field collected samples were used in the study.
Ethics oversight	All experiments were conducted in accordance with University of Washington's Institutional Animal Care and Use Committees.

Note that full information on the approval of the study protocol must also be provided in the manuscript.

Plants

Seed stocks	N/A
Novel plant genotypes	N/A
Authentication	N/A